Journal of Hydrology 651 (2025) 132595

Contents lists available at ScienceDirect

Journal of Hydrology

journal homepage: www.elsevier.com/locate/jhydrol

Eco-hydrological recovery following large vegetation disturbances from a mega earthquake on the eastern Tibetan plateau

Jiehao Zhang [a,b,c], Yulong Zhang [c,d,*], Matthew P. Dannenberg [e], Qinfeng Guo [c], Jeff W. Atkins [f], Wenhong Li [d], Ge Sun [c]

[a] Wuhan Botanical Garden, Chinese Academy of Sciences, Wuhan 430074, China
[b] Department of Land Resources Administration, China University of Geosciences, Wuhan 430074, China
[c] Eastern Forest Environmental Threat Assessment Center, USDA Forest Service, Research Triangle Park, NC 27709, USA
[d] Division of Earth and Climate Sciences, Nicholas School of the Environment, Duke University, Durham, NC 27708, USA
[e] Department of Geographical and Sustainability Sciences, University of Iowa, Iowa City, IA 52245, USA
[f] USDA Forest Service, Southern Research Station, New Ellenton, SC 29809, USA

A R T I C L E I N F O

Keywords:
Vegetation disturbance
Earthquake
Casual impact analysis
Eco-hydrological modeling
Evapotranspiration
Gross primary productivity

A B S T R A C T

Catastrophic earthquakes induce significant, enduring vegetation disturbances through extensive landslides and geomorphological alterations. The post-earthquake vegetation recovery hinges on the disturbance severity, climatic variability, and strategic human intervention, yet understanding of these critical processes and their influences on eco-hydrological functions at the landscape level remains limited. This study aims to quantify the earthquake's impacts on vegetation structure and eco-hydrological functions and to elucidate the recovery mechanisms driven by climate variability and human efforts. We focused on the 2008 Wenchuan Earthquake on China's eastern Tibetan plateau as a case study to investigate its influences on vegetation cover and eco-hydrological functions in gross primary productivity (GPP), evapotranspiration (ET) and water yield (WY) using remote sensing, spatial-resolved causal impact analysis, and ecohydrological modeling. We found that the earthquake caused widespread vegetation disturbances from 2008 to 2010, altering land cover over 12% of the study area, and reducing GPP and ET by 7.0% and 14.7%, respectively. During this period, the affected regions witnessed a larger variation in WY, primarily due to a decrease in ET. From 2010 to 2018, GPP and ET showed rapid recovery, driven by both climatic factors (accounting for 23%-56% of the recovery), and human intervention (contributing 30%-42% to the recovery). Though WY did not show a statistically significant trend, human intervention-induced ET change was responsible for 38.9% to the changes in WY during the recovery period. Nevertheless, by 2018, 45% of the affected area still had not returned to pre-earthquake levels, with recovered areas remaining below the projected non-earthquake levels, indicating the vulnerability of mountainous ecosystems in recovery. Our findings highlight the significant, long-lasting eco-hydrological impacts of a catastrophic earthquake and underscore the effectiveness of integrating natural regeneration with targeted human restoration efforts. These insights improve our understanding of ecological vulnerability and resilience following natural hazards, providing valuable guidance for future post-natural disaster restoration initiatives.

1. Introduction

Acute natural hazards, such as earthquakes, volcanic eruptions, wildfires, and extreme floods, can catalyze abrupt and dramatic vegetation disturbances (Scholes et al., 2018). Such immediate disturbances could strongly alter ecosystem structure and function (Allen et al., 2020; Garwood et al., 1979; Lin et al., 2023) and lead to complex trajectories in post-disaster vegetation recovery within the context of climate change and anthropogenic activity (Chen et al., 2021; Gan et al., 2019). Understanding how earthquakes affect vegetation and to what degree ecosystems recover from such disturbances is crucial for assessing ecosystem resilience to natural disturbances (Seidl and Turner, 2022). This knowledge can inform disaster preparedness and response strategies, helping better manage and recover from hazards-related ecological disruptions (Logan et al., 2022).

The eco-hydrological ramifications of earthquakes are significant,

* Corresponding author.
E-mail address: yulong.zhang@duke.edu (Y. Zhang).

https://doi.org/10.1016/j.jhydrol.2024.132595
Received 24 March 2024; Received in revised form 14 October 2024; Accepted 8 December 2024
Available online 25 December 2024

simultaneously affecting vegetation cover, geomorphology and a variety of eco-hydrological dynamics related to ecosystem productivity, evapotranspiration, water yield and stream flows (Allen et al., 2020; Duan et al., 2021). Initially, earthquakes physically alter the landscape, primarily through landslides following the main shock. The aftermath of an earthquake leads to changes in shallow sedimentation, ground fissures, and vegetation disruption, culminating in sediment accumulation in a quasi-stable state during dry seasons (Lin et al., 2023), which is prone to reactivation in rainy periods (Yang et al., 2021). As a result, there is generally an increase in the frequency of post-earthquake geological hazards that potentially destroy vegetation cover (Khan et al., 2013; Li et al., 2018). The damaged or degraded vegetation not only reduces regional carbon sequestration capacity (Peng et al., 2013), but also decreases the buffering of rainfall onto the soil and reduces the amount of water transpired back into the atmosphere, thus leading to increased surface runoff (Ma et al., 2017; Zhang et al., 2021a). This can result in further erosion and loss of fertile topsoil, resulting in diminished plant habitat quality (Deng et al., 2010), and increasing the risk of subsequent landslides and affecting local water resources. In densely populated areas, earthquakes typically trigger human intervention such as post-disaster resettlement and reconstruction projects, which may positively influence the surrounding vegetation (Peng and Fu, 2018). Understanding these vital eco-hydrological processes is essential for comprehending the resilience and recovery of ecosystems following earthquakes.

Quantifying the impact of earthquakes and recovery policies on post-earthquake vegetation is challenging due to multiple complex factors, including the disturbance's severity (Allen et al., 2020), climate variability, and diverse human management practices (Wang et al., 2022). Even in the absence of external disturbances, vegetation naturally undergoes continuous growth due to intrinsic succession. Consequently, it is challenging to separate climatic influences and the direct effects of earthquake disturbances to ecosystem function. Furthermore, determining the role of human intervention in the vegetation recovery process following seismic disturbances is key to better understanding the mechanisms of vegetation restoration. Some studies have solely employed empirical comparative (Pandey et al., 2022) or statistical (Duan et al., 2021) analysis to separate the effects of human and natural factors. However, these methods struggle to causally test the direct impact of earthquakes and human interventions on vegetation dynamics following an earthquake. The integration of remote sensing and ecological models is crucial in this context. Remote sensing enables the detailed observation of vegetation at the landscape level (Crowley and Cardille, 2020), capturing the trajectories of disturbances and recovery processes, while ecological models could further simulate eco-hydrological functions behind these dynamics. Causal impact analysis (CIA) offers a robust approach to isolate and quantify the causal impacts of specific events or interventions, making it a valuable complementary method for remote-sensing based ecological simulations (Brodersen et al., 2015). Although primarily applied to economics and social sciences, the adoption of CIA in eco-hydrology, particularly for examining sudden events like earthquakes at the landscape scale, remains limited (Brodersen et al., 2015).

The 2008 Wenchuan earthquake, a significant seismic event in China's eastern Tibetan plateau, instigated widespread land surface alterations. Vegetation deterioration ensued persistently for years following the seismic shock (Gan et al., 2019). Secondary geological disasters, such as landslides and mudslides induced by the earthquake, directly damaged extensive tracts of vegetation (Bao, 2008; Bao and Pang, 2008). Some counties near the earthquake's epicenter experienced vegetation losses exceeding 20 % (Bao, 2008; Ouyang et al., 2008). Following the earthquake, China launched an ambitious reconstruction initiative aimed at mitigating soil erosion and the restoration of ecosystem services within a three-year span. More than a decade later, the post-Wenchuan period offers a valuable opportunity for a comprehensive assessment on the long-term impacts of this mega earthquake on ecosystem structure and eco-hydrological function.

Here, we aim to understand the earthquake-induced vegetation cover change and the subsequent recovery in eco-hydrological functions, specifically gross primary productivity (GPP), evapotranspiration (ET), and water yield (WY), in the context of climate variability and human management. Using the remote-sensing-driven Coupled Carbon and Water (CCW) ecosystem model, we simulated monthly carbon and water fluxes (GPP, ET and WY) from 2001 to 2018, encompassing the pre- and post-earthquake periods over the affected zone. Through spatial-resolved CIA and controlled model experiments, we investigated the mechanisms behind the disruption and subsequent recovery of vegetation function following the earthquake, focusing on three main questions: (1) How did the earthquake immediately alter vegetation cover, GPP, ET and WY at the spatial scale? (2) To what degree did the vegetation cover, GPP, ET and WY revert to their pre-earthquake states after a decade of recovery? (3) How did the earthquake, subsequent human intervention, and climatic variability—specifically changes in solar radiation, temperature, and water stress—individually and collectively influence the post-quake dynamics of GPP, ET and WY? By addressing these questions, we expect to enhance our understanding of ecosystems response to earthquake disturbances and their recovery under intensive human interventions, thus informing effective ecosystem management practices and contributing to the broader discourse on ecological restoration and conservation, particularly in the context of natural disturbances and climate change.

2. Materials and methods

2.1. Study area

The devastating Wenchuan Earthquake hit the Sichuan province of China on May 12, 2008, with a magnitude of 8.0 at the Richter scale. It was one of the deadliest earthquakes in China's recorded history, causing widespread destruction and leading to the deaths of over 69,000 people, with tens of thousands missing or injured. The earthquake left roughly 4.8 million people homeless, impacting 417 counties in 10 provinces. Particularly hard-hit were ten counties in Southwest China within an area of about 26,000 km2, straddling the boundary between the Tibetan Plateau and the Sichuan Basin (Fig. 1a), categorized as the extremely affected area (EAA) by the United Nations Centre for Regional Development (UNCRD, 2009). The earthquake's epicenter was situated in the southwest of the study area (Fig. 1a). The most severe seismic intensity was observed along a southwest-northeast axis with a length of 300 km and a width of 50–80 km (Fig. 1a) (Bao and Pang, 2008; UNCRD, 2009). The EAA's topography features significant variations in elevation, ranging from a peak of 5300 m to a low of 490 m (Fig. 1a) with slope range 0–37 % (Fig. S2). Most of the study area is mountainous, with only a small portion of plains, primarily located in the southeast. The area is in a transitional zone that ranges from a mountainous subtropical to a highland climate, with an average annual (referring to one solar year, same below) precipitation of 600–900 mm and an average annual temperature of 12–16 °C. The complex terrain results in highly heterogeneous climatic conditions, with temperature, precipitation, and solar radiation varying greatly across the landscape. The high mountains stand on the western edge of the Sichuan Plain (Fig. 1a), which intercepts the warm and humid airflow from the southeast during the summer months. Consequently, the eastern mountain slopes receive more than 1000 mm of annual precipitation, whereas the western slopes experience arid to semiarid conditions, with annual precipitation ranging from 500-700 mm (Fig. S2).

The land cover within the EAA is closely tied to elevation gradients. By 2018, croplands were mainly distributed in the lower-lying plains of the southeast, covering 7 % of the study area (Fig. 1b). Shrublands occupied 24 % of the study area, mainly distributed in the northeast's low-elevation valley and higher elevations of the central mountains. Forests, constituting 53 % of the land cover, were mainly distributed in

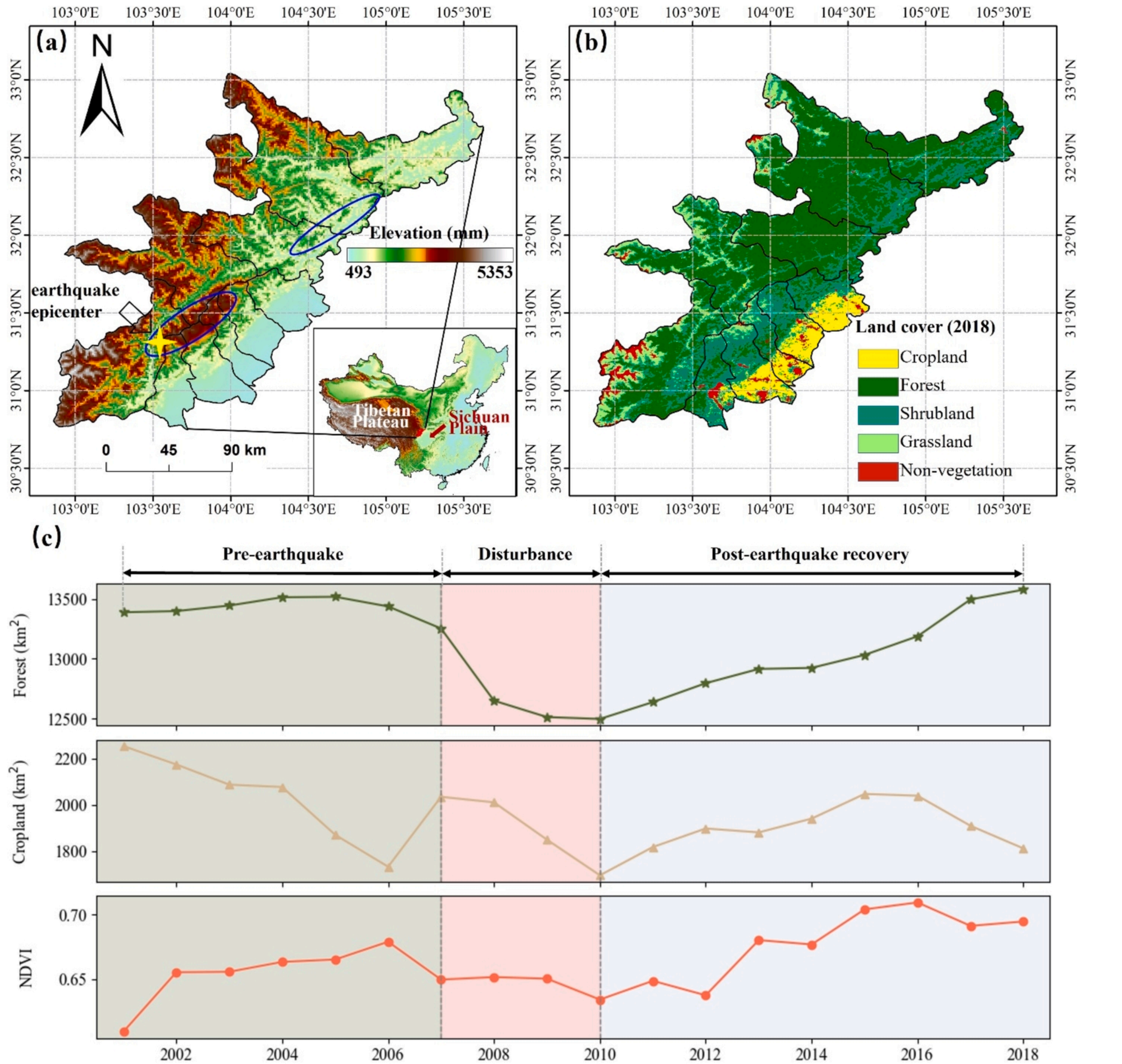

Fig. 1. Spatial patterns of terrain feature (a), land cover in 2018 (b), and annual vegetation dynamics of the whole study area during three distinct phases (pre-earthquake period, disturbance period and vegetation recovery period) from 2001 to 2018 (c). In (a), the yellow star indicates the earthquake epicenter, and the blue ellipses denote areas with the highest seismic intensity. Black lines in (a) and (b) denote county boundaries. In (c), the pre-earthquake period is defined as 2001–2007, the disturbance period as 2008–2010, and the post-quake recovery period as 2011–2018. The annual values for each vegetation cover (forest and cropland) are the area of each land cover type at the end of each year and the mean annual NDVI for the entire study area.

the northern and middle mountainous areas. Grasslands made up 13 % of the area, occurring primarily at the highest elevations (Fig. 1b). Non-vegetated areas included urban expanses (in the southeast plains) and glacier peaks (Fig. 1b).

2.2. Phases of vegetation dynamics before and following the earthquake

The Wenchuan earthquake caused a series of complex abrupt and intermittent changes in vegetation structure and functions (Bao, 2008; Bao and Pang, 2008). The alteration due to the earthquake was not a singular event but emerged as a prolonged process. The primary earthquake and its aftershocks in mountainous areas not only brought immediate damage to the vegetation but also triggered large numbers of landslides that later influenced vegetation. These landslides deposited loose rocks and debris on the hillslopes, making these areas prone to further erosion and landslides, especially during rainfall events. This ongoing geological instability led to the continuous destruction of vegetation (Lin et al., 2004; Marc et al., 2015; Zhang et al., 2017), although it gradually diminished over time (Fan et al., 2018; Li et al., 2018; Tang et al., 2016). A pre-analysis of land cover data revealed a continuous decline in the forest, cropland coverage, and NDVI up to three years following the earthquake (Fig. 1c). Based on these observations, we therefore divided the study period into three distinct periods: the pre-earthquake period (2001–2007), the disturbance period (2008–2010), and the recovery period (2011–2018) (Fig. 1c). The pre-earthquake period served as a baseline for ecological conditions, with vegetation in a relatively undisturbed state, providing a reference point to gauge the extent of changes induced by the earthquake. The initiation of the disturbance period was marked by the mainshock and subsequent aftershocks, leading to gradual yet significant alterations in the vegetation. Following this, the recovery period, which began after 2010, was characterized by the gradual recuperation and regeneration of vegetation in the context of climate variability and human intervention aimed at restoring the affected ecosystems mainly via artificial grass and tree planting. In addition, agricultural production and agro-ecosystems were gradually recovering in tandem with the broader recovery of human society.

2.3. Coupled carbon and water model

The satellite-based Coupled Carbon and Water (CCW) model estimates gross primary productivity (GPP) and evapotranspiration (ET) at a monthly scale in a unified framework (Zhang et al., 2016, 2019b). Central to the model's design is its carbon-centric strategy, with ET calculations guided by GPP in conjunction with a conservative underlying water-use efficiency (UWUE) (Zhou et al., 2014). Such a framework not only avoids full simulation of the soil water balance, which is still a significant challenge in hydrological modeling, but also captures the critical coupling between carbon uptake from photosynthesis and water loss via transpiration (Zhang et al., 2016). CCW has been calibrated with site-level observations from global FLUXNET data (Pastorello et al., 2020) and extensively applied to quantify carbon and water dynamics for global terrestrial ecosystems (Dannenberg et al., 2021; Zhang et al., 2019a,b), large river basins like the Yangtze River Basin (Zhang et al., 2022), and smaller watersheds like the Han River Basin (Zhang et al., 2021). The key equations for GPP, ET and WY calculations in CCW are shown below:

$$GPP = APAR \times \varepsilon = (PAR \times FPAR) \times \left(\varepsilon_{pot} \times R_s\right) \times (T_s \times W_s) \quad (1)$$

$$FPAR = 1.24 \times \mathrm{NDVI} - 0.168 \quad (2)$$

$$ET = \frac{GPP \times VPD^{0.5}}{UWUE} \quad (3)$$

$$WY = \mathrm{P} - \mathrm{ET} \quad (4)$$

where APAR is the absorbed photosynthetically active radiation ($\mathrm{MJ \cdot m^{-2}}$), representing the amount of energy absorbed by plant canopies for photosynthesis; PAR is the incident photosynthetically active radiation at the top of vegetation canopy, which is assumed to be 45 % of the total shortwave radiation (Running et al., 2000); FPAR is the fraction of PAR absorbed by plant canopies, estimated from satellite-based normalized difference vegetation index (NDVI);ε_{pot} ($\mathrm{g \cdot C\ MJ^{-1}}$) is the potential LUE under optimal conditions; R_s, T_s and W_s are environmental scalars for diffuse radiation, temperature, and moisture stresses, each ranging from 0 to 1; VPD (hPa) is vapor pressure deficit; UWUE, representing the trade-off between carbon gain and water loss, was estimated from FLUXNET data (Pastorello et al., 2020) and varied from 4.5 to 8.4 g C $\mathrm{kg^{-1}}$ H_2O across land cover types; WY is water yield, which is derived by the difference between precipitation (P) and ET. WY represents the available water supporting for both surface and groundwater flows. All CCW model parameters were calibrated for specific biomes, making it particularly adept at assessing the impacts of vegetation structure and function changes induced by large-scale disturbances, such as earthquakes.

The CCW model was previously calibrated and validated based on global flux data (Zhang et al., 2019b, 2016). According to Zhang et al (2019b), CCW captured 71 % of site-level GPP variations at the global scale, and showed robust predictions in different ecosystems at the regional scale and comparative performance with a series of existing light-use efficiency models. Here, we mainly focused on the evaluation of ET by CCW. We first compared CCW ET with hydrological observations in the Mintuo and Jialing River basins, two sub-basins of Yangtze River Basin (Fig. S2). Annual data on total stream flow (Q) and precipitation (P) spanning from 2001 to 2018, sourced from the Water Resources Bulletin of the Yangtze River Basin and Southwest Rivers, provided a basis for calculating ET using the water balance approach (ET = P – Q) by assuming the soil water storage change as zero at the annual scale. This assumption is generally accepted in this subtropical region due to relatively fast hydrological exchanges (Han et al., 2020) and stable groundwater storage (Long et al., 2015). However, we acknowledge that this method may introduce uncertainties in the evaluation. ET simulations by CCW were then compared to the water balance-derived ET for both sub-basins. We evaluated CCW-simulated ET using the performance indicators of the coefficient of determination (R^2), root mean squared error (RMSE), and mean bias error (MBE). Overall, the CCW model showed strong predictive capacity, capturing 86 % of the observed interannual variability in ET ($R^2 = 0.86$) and exhibiting only a modest systematic overestimation (MBE = 15.2 mm) and an RMSE of 48.2 mm (Fig. 2a).

In our previous work, we evaluated CCW at regional scale over the Yangtze River Basin of China (Zhang et al., 2022), where the study area is located, using five published ET data products derived with different algorithms (Table S1), as well as hydrological gauges from 15 small watersheds (Table S2). It shows that annual ET from CCW had a good consistency for four of the five ET products for the whole Yangtze River Basin, particularly the microwave-based ET product of GLEAM and process-based ET product of PML-V2 (Fig. 2b). In addition, CCW ET captured 90 % of variations in annual ET derived from P-Q over 15 small watersheds ($R^2 = 0.90$) with an RMSE of 62.9 mm (Fig. S2). Therefore, we concluded that CCW is suitable for our regional eco-hydrological study.

2.4. Remote sensing and climate data

We use a combination of remote sensing and climate data to facilitate the operation and analytical simulations of the CCW model. Annual, 500-m resolution land cover dynamics from 2001 to 2018 were obtained from the MODIS product (MCD12Q1 V6) (Sulla-Menashe et al., 2019). The biome-specific parameters of CCW were determined based on the 17 International Geosphere-Biosphere Programme (IGBP) land cover classes, combined into five general types: forest (including evergreen, deciduous, mixed forests), shrubland (including open and closed shrublands, savannas, and woody savannas), grassland, cropland, and non-vegetated (i.e. urban land, barren land, and water). Monthly NDVI data, used for estimating FPAR, were obtained from the MODIS MOD13A1 product (V6) for the same period at 500 m spatial resolution. To minimize cloud contamination, the original 16-day data was gap-filled with TIMESAT 3.2 (Jönsson and Eklundh, 2004) and then averaged to the monthly scale.

As for climatic factors, we used monthly precipitation (P), air temperature (T), VPD, and shortwave radiation (SR) from 2001 to 2018 from the TerraClimate dataset (Abatzoglou et al., 2018). Given the absence of mean air temperature, we calculated it by averaging monthly maximum and minimum temperatures. Previously, we confirmed a high degree of agreement between TerraClimate's precipitation and temperature data and observed climate data over the Yangtze River Basin of China, with strong coefficients of determination (R2) of 0.97 for precipitation and 0.99 for temperature, respectively (Zhang et al., 2022). To match other model's inputs, the TerraClimate data were downscaled from their ~ 4 km spatial resolution to a finer 500-m grid using the cubic convolution resampling method.

2.5. Analysis methods

2.5.1. Recovery index

To quantify the recovery of vegetation cover and eco-hydrological function following the earthquake, we introduced a Recovery Index (RI). This index is defined as the ratio of restored values to lost values for

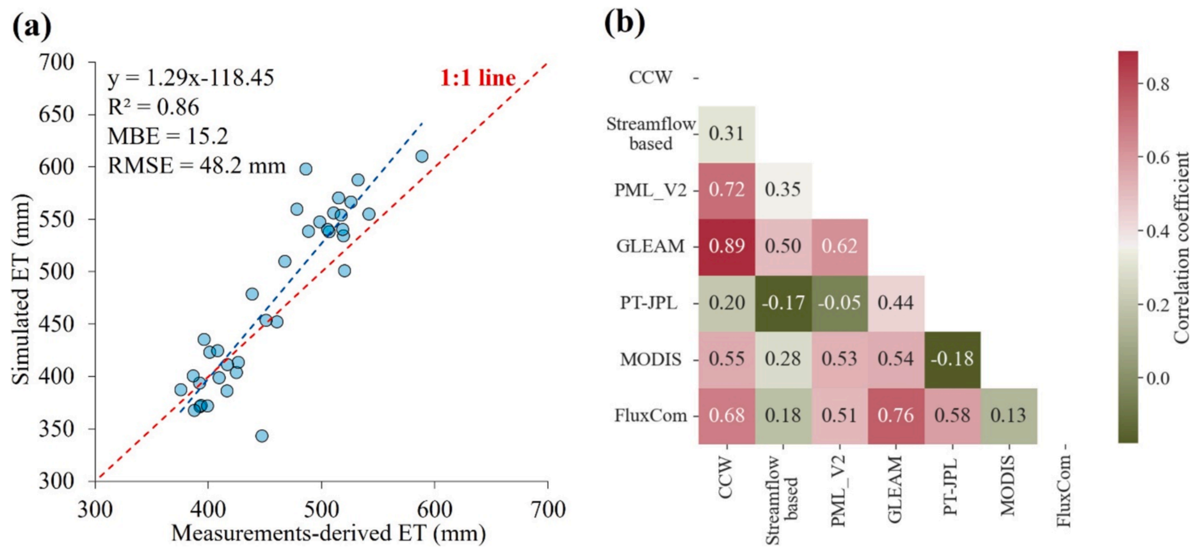

Fig. 2. Evaluation of CCW-simulated ET based on different source of ET estimation. (a) Scatter of annual CCW ET and annual ET derived from a water balance approach (P-Q) for the two basins within the study area (Fig. S2). (b)Correlations matrix among CCW-based ET, streamflow-based ET (P-Q) and ET from five data products (Table S1) over Yangtze River Basin, where the study area is located (Fig. S2).

vegetation (NDVI) and eco-hydrological function proxies (GPP, ET and WY) between the recovery period (2011 to 2018) and the disturbance period (2008–2010). We assessed disturbance extent by calculating the deviation of 2010 values from the pre-earthquake average for each indicator. The recovery magnitude was determined by multiplying the linear growth rate of each indicator throughout the recovery period by the recovery duration, which spanned 8 years.

2.5.2. Causal impact analysis and scenario experiments

Causal impact analysis (CIA) is a statistical approach for estimating the causal effect of specific events or intervention on target outcomes (Brodersen et al., 2015). The primary goal of the CIA is to isolate and quantify the impact of an event or intervention while controlling for other factors that might influence the outcome. CIA employs a Bayesian structural time-series (BSTS) model to estimate the causal effect of an intervention in time-series data (Brodersen et al., 2015). Specifically, BSTS employs a diffusion regression state-space approach to predict counterfactual trends in synthetic control scenarios. These trends represent what would occur in a hypothetical situation without intervention—thus, in a scenario where no earthquake occurred. The model estimates the causal impact of an intervention (i.e. an earthquake) by comparing the actual time series data of the variable of interest (i.e. NDVI) with the counterfactual scenario where the intervention did not take place (Brodersen et al., 2015). BSTS is defined by two state-space model equations. The first, the observation equation, is:

$$y_t = Z_t^T \alpha_t + \varepsilon_t \tag{5}$$

where y_t is the scalar observation, Z_t is the d-dimensional output vector, and $\varepsilon_t\ N(0, \sigma_t^2)$ is the scalar observation error with variance σ_t. The observation equation links the observed data y_t to the latent d-dimensional state vector α_t. The second equation, the state equation, is:

$$\alpha_{t+1} = T_t \alpha_t + R_t \eta_t \tag{6}$$

where T_t is the d × d transition matrix, R_t is the d × q control matrix, and η_t is the q-dimensional system error with q × q state diffusion matrix Q_t, such that $\eta_t\ N(0, Q_t)$. This equation governs the dynamic evolution of the state vector α_t over time. For implementation, we rely on the CausalImpact package provided in R (Brodersen et al., 2015). Each model was fitted by considering a single target time series, which maps the trend of NDVI over the considered time window. Each model includes a seasonal component, set to one year per cycle, with May 2008 as the point of intervention. In this study, we conducted CIA at the landscape scale through four steps: (1) Identifying Earthquake-impacted pixels: We scrutinized the spatial distribution of NDVI alterations to pinpoint vegetation pixels manifesting a consistent NDVI decline during the disturbance period (Fig. 3a); (2) Extracting NDVI time series of earthquake impacted pixel and non-impacted pixels: For each earthquake-impacted pixel, we extracted 16-day NDVI time series of non-impacted pixels within a 10 km (20 pixels) radius (Fig. 3b); (3) Performing CIA: we compared the NDVI time series of earthquake-impacted pixels (response series) with those from non-affected areas (control series) within a 10-km radius to simulate counter-factual NDVI dynamics of the earthquake-impacted pixels in the absence of the earthquake (Fig. 3c) using the R package CausalImpact (Brodersen et al., 2015); (4) Investigating and attributing GPP and ET dynamics: We conducted two model scenario experiments to explore factors affecting GPP and ET recovery (Fig. 3c):

Scenario A: Simulating actual changes of GPP and ET by incorporating dynamic changes in all variables throughout the study period. We assumed that GPP and ET fluctuations arose from a combination of factors, including both the direct and indirect impacts of earthquakes between 2008 and 2010, and human intervention from 2008 to 2018 in the background of climate variability throughout the whole period.

Scenario B: Simulating GPP and ET under the hypothetical scenario where no earthquake occurred, using NDVI forecasts from the spatial-resolved CIA and keeping land cover constant at its 2007 level, while allowing for climatic changes. This scenario posits that vegetation would progress naturally in an undisturbed setting, with all changes exclusively attributed to climatic factors.

By calculating the differences of GPP, ET and WY between Scenario A and B (A minus B), we can assess the influence of the earthquake during the disturbance period (2008–2010) and the role of human intervention during the recovery period (2010–2018) because climate effects during these two scenarios can be cancelled out. However, we recognize that the effect of human intervention here is superimposed on intrinsic vegetation regrowth, which cannot be completely isolated in our study. Overall, this approach enables the quantification of the relative contributions of the earthquake, human intervention, and climatic variability to the observed changes in GPP, ET and WY, based on the proportion of their impacts to the overall effects.

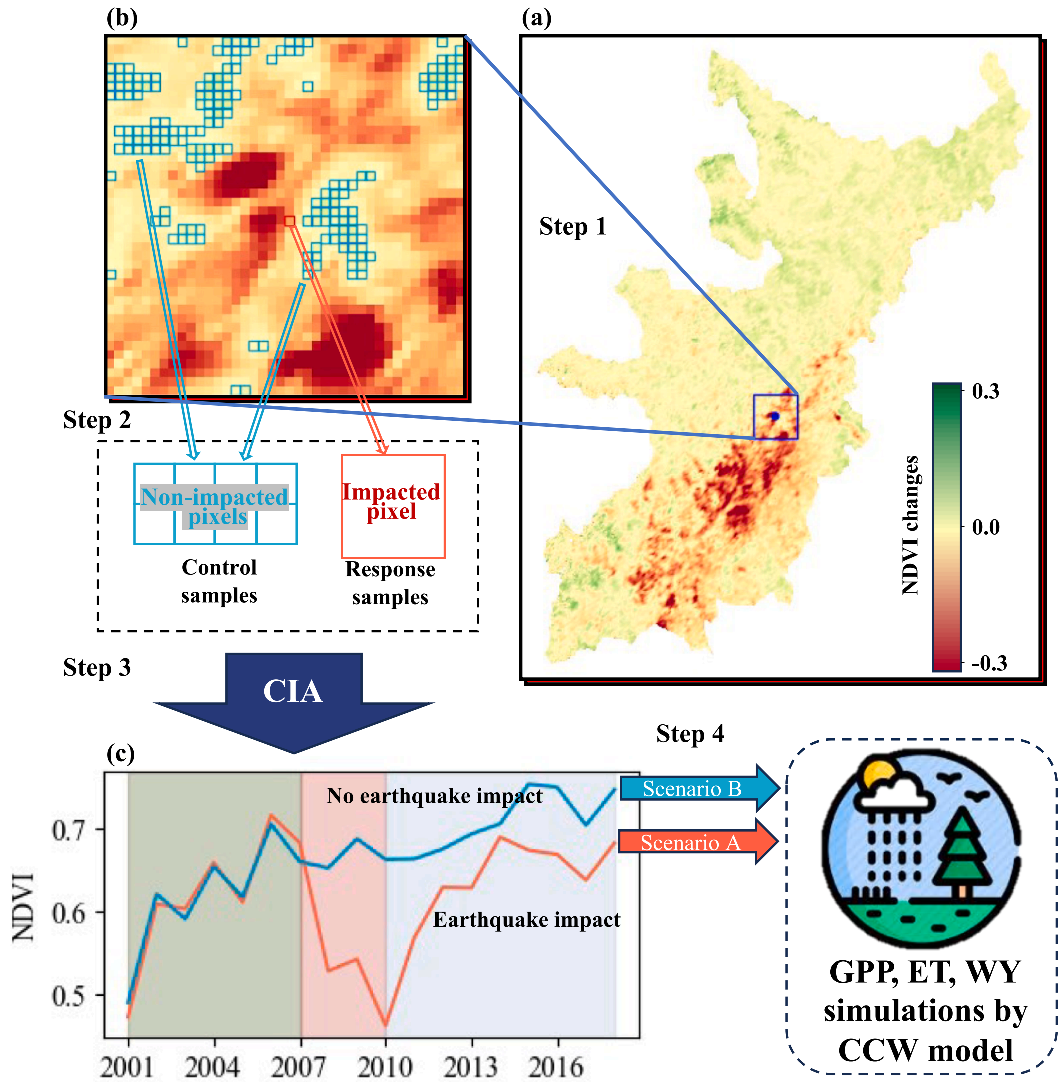

Fig. 3. An example of spatial-resolved causal impact analysis (CIA) and scenario simulation in four steps. (a) Spatial distribution of annual NDVI changes in 2010 relative to 2007, where the blue square represents the corresponding 10 × 10 km windows around the earthquake-affected target pixel (blue dot) as an example. b) Spatial distribution of annual NDVI anomaly within the sampling window with the red-framed pixel being the earthquake-affected vegetation and the blue-framed pixels being the non-earthquake-affected vegetation. (c) Actual NDVI time series for the target pixel alongside the CIA-predicted NDVI time series by consuming no earthquake influence based on the relationship between those unaffected pixels and the target pixel before earthquake. The actual and CIA-based simulated NDVI are then feed to the CCW model to quantity the earthquake-induced GPP, ET and water yield (WY) changes in Step 4.

3. Results

3.1. Vegetation cover changes following earthquake

We observed rapid declines in both forest and cropland cover following the Wenchuan earthquake (Fig. 1c, 4b). During the disturbance period (2008 to 2010), land cover change occurred over 12 % of the total study area (Fig. 4b). Forest cover suffered the largest loss, with a notable decrease in 2008, continuing through 2009 and 2010 (Fig. 1c), leading to a total reduction of 831.3 km^2 (3.2 % of the total area). Meanwhile, cropland declined by 338.2 km^2 (1.3 % of the total area), mostly changing to grassland. Forest reduction was concentrated in the central mountainous area (Fig. 4b), while cropland decline was more pronounced in the southeast plains (Fig. 3b). Vegetation cover rapidly recovered after 2010, particularly in cropland and forest areas, which had been most adversely affected during the earthquake. The cropland area, at its lowest in 2010 (1697.3 km^2), rebounded to a peak of 2048.0 km^2 in 2015, surpassing both its 2007 extent (2035.5 km^2) and pre-earthquake average (2033.8 km^2) (Fig. 1c). Forest cover also grew after reaching its lowest level in 2010 (12,497.8 km^2), surpassing pre-earthquake levels by 2017 and continuing to increase in 2018, mainly at the expense of shrubland. Most new cropland was in the southeastern plains, while the forest expanded mainly in the central and western mountains.

The earthquake impact area experienced a sharp decrease in annual mean NDVI from 0.65 in 2008 to 0.59 in 2010 but rebounded rapidly at a rate of 0.012 per year ($P < 0.01$) in the post-earthquake period (Fig. 4d). In contrast, the NDVI of areas unaffected by the earthquake increased during 2008–2010 at a rate of 0.006 per year ($P < 0.05$) (Fig. 4d). The spatial pattern of NDVI changes showed high heterogeneity (Fig. 4a, 4b). During 2007–2010, 47.5 % of the total area experienced a decrease in NDVI, with 9.0 % showing a substantial drop of at least 0.1, predominantly in the central mountainous area (Fig. 4a). During the recovery period, increased NDVI occurred across 93 % of the study area. The central mountains, severely impacted by the earthquake, registered a mean NDVI increase greater than 0.2. Remarkably, the NDVI of about 90 % of the damaged area at least partly recovered after the earthquake, with 70 % reverting to pre-earthquake NDVI or greater

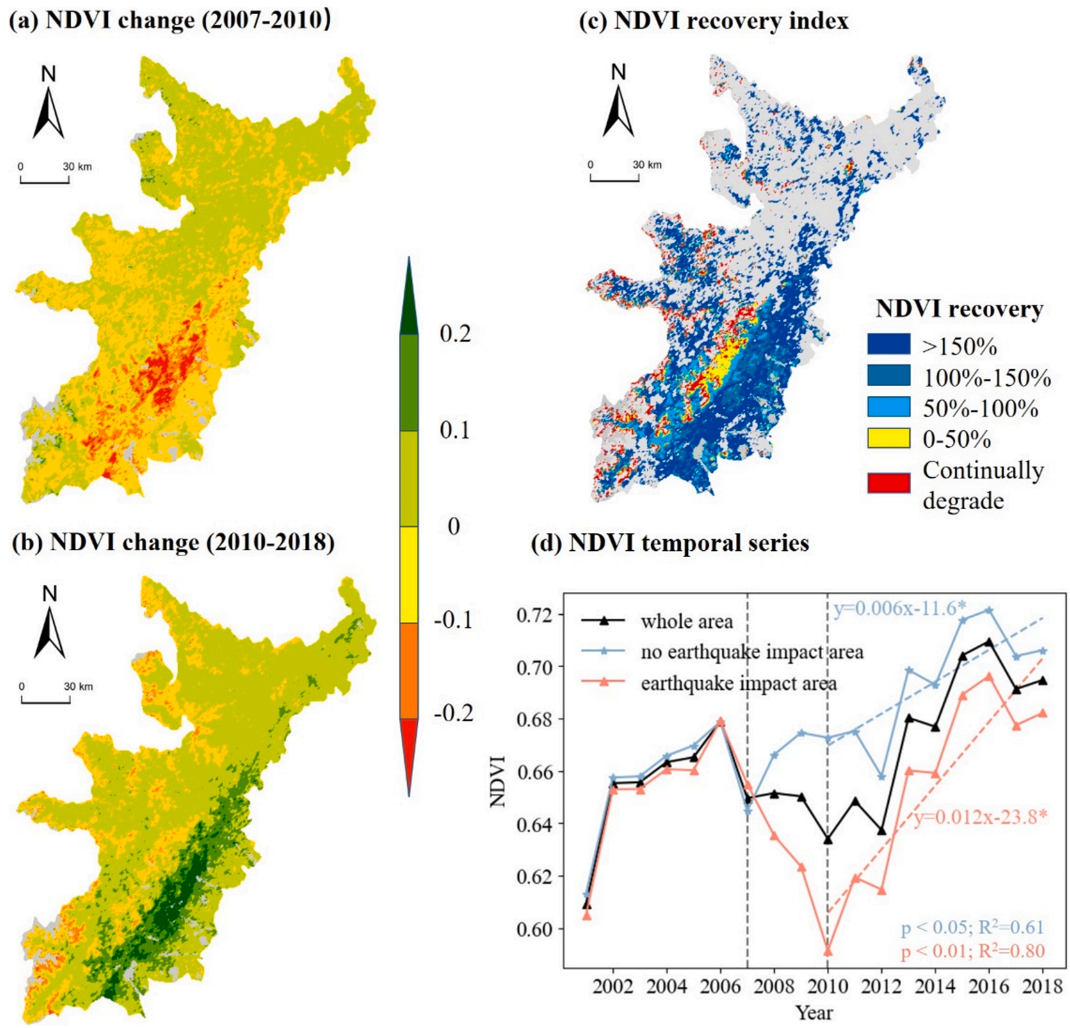

Fig. 4. Earthquake-induced spatial and temporal changes in vegetation greenness in terms of NDVI. (a) Spatial distribution of annual NDVI change during the disturbance period (2007–2010) and (b) post-earthquake vegetation recovery period (2010–2018), and (c) vegetation recovery index between these two periods. (d) Annual NDVI dynamics over the whole study area, earthquake impact area, and no earthquake impact area during 2001–2018. The terms "continually degrade" in (c) refer to earthquake impact regions with NDVI continually decreasing in the recovery period. Dashed vertical lines in (d) delineate the three phases of vegetation dynamics during the study period: pre-earthquake (2001–2007), disturbance (2008–2010), and recovery (2010–2018). "*" in (d) means the trend is statistically significant ($P < 0.10$).

(Fig. 4c). More than half of the affected vegetation cover (55 %) even recovered by more than 150 % (Fig. 4c). However, there remained 10 % of the damaged vegetation that continued to degrade after the earthquake, mainly on the west side of the central mountains and in higher elevation areas (Fig. 4c).

3.2. GPP, ET and WY changes following earthquake

The earthquake led to large declines in GPP and ET (Fig. 5). Relative to 2007, annual GPP and ET in 2010 over the whole study area decreased by 102.95 g $C/m^{-2}(-|-)$ (7.0 %) and 73 mm (14.7 %), respectively (Fig. 5a, b). Within the earthquake impact area, both GPP and ET declined sharply. Conversely, in the unaffected regions, annual ET only slightly decreased while GPP increased slightly. Overall, annual GPP and ET decreased in 69.2 % and 94.2 % of the study area, respectively (Figs. S3).

Vegetation function recovered rapidly after the earthquake, with increases of 198.2 g $C/m^{-2}(-|-)$ in annual GPP and 87.2 mm in annual ET from 2010 to 2018, respectively (Fig. 5a, b). Spatially, 93.4 % of the area showed a positive GPP trend during this recovery period (Fig. S3), with significant increases ($P < 0.1$) observed in 43.2 % of the total area, mainly in the central mountainous area and the western river valley (Fig. S3). Similarly, ET rose over 94.4 % of the study area (Fig. S3), with significant trends in 28.1 % of the total area. Only a small fraction (6.6 % of the total area for GPP and 5.6 % for ET) showed declining trends during the post-earthquake recovery period (Fig. S3), mostly in high elevation area. With the combined effects of land cover change and climate variability, GPP and ET at least partly recovered over about 95 % of the study area (Fig. 5c, d). Specifically, 72 % of the GPP affected area and 55 % of the ET affected area recovered to, or even exceeded, pre-earthquake levels (Fig. 5c, d). Notably, about 54 % of GPP affected area and 30 % of ET affected area recovered by more than 150 % of the damage (Fig. 5c, d).

During the earthquake disturbance period, the affected regions experienced a significant increase in water yield (WY), primarily due to a decrease in evapotranspiration (ET). Prior to the earthquake, WY exhibited considerable interannual variability, generally corresponding with precipitation variations. However, we found that post-earthquake, WY became more sensitive to changes in precipitation (Fig. 6a). From 2007 to 2010, the variation in WY (179.2 mm) was significantly greater than the variation in precipitation (71.3 mm), with a difference of 107.9 mm (151 % of precipitation variation) (Fig. 6a). This discrepancy was

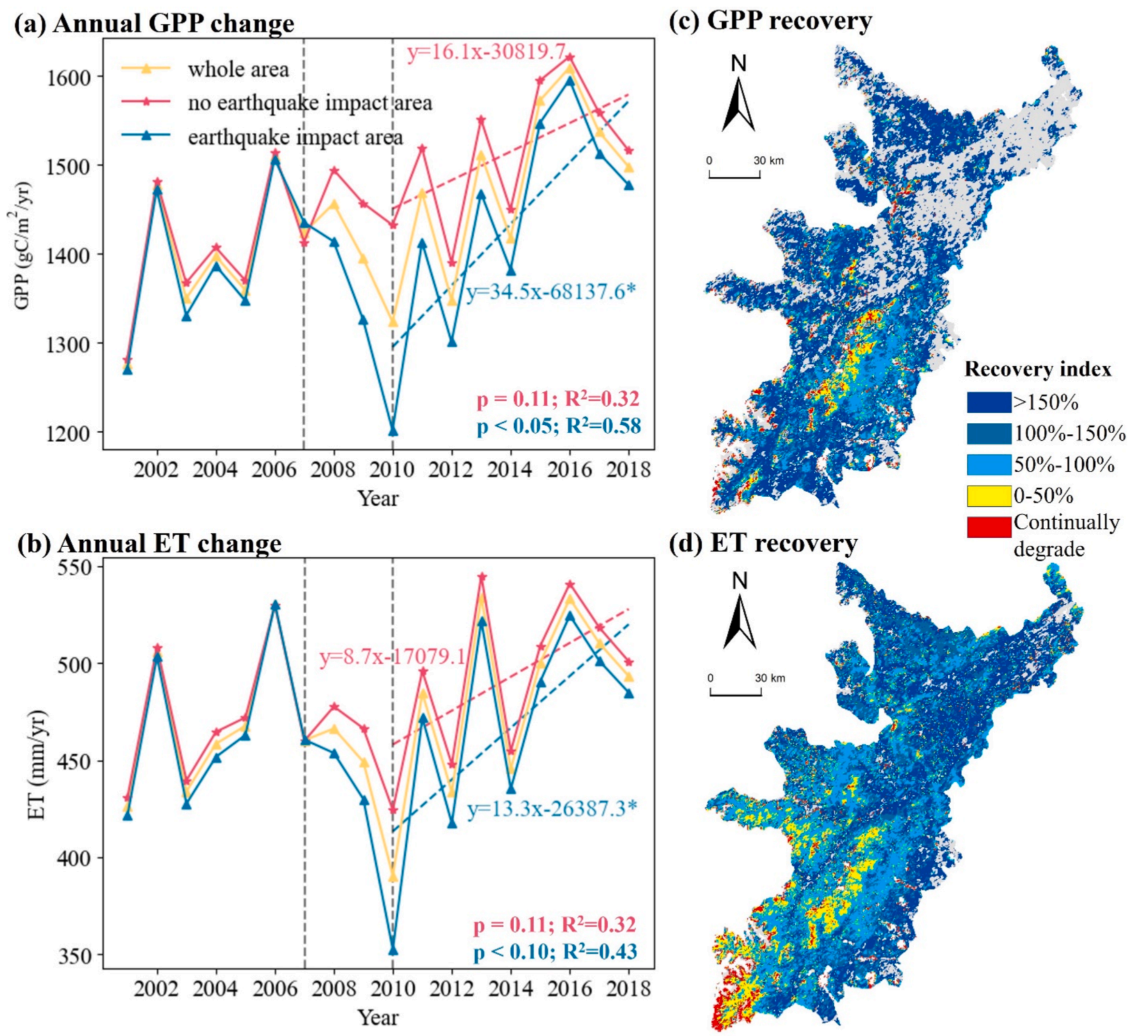

Fig. 5. Earthquake-induced spatial and temporal changes in GPP and ET. Annual mean GPP (a) and ET (b) in the whole study area, earthquake impact area, and no earthquake impact area during 2001–2018; spatial distribution of recovery index of GPP and ET (c, d). Dashed vertical lines in (a) and (b) delineate the three "phases" of land cover transition during the study period: pre-earthquake (2001–2007), disturbance (2008–2010), and recovery (2010–2018). The gray areas in (c) and (d) are regions where no significant changes were observed in GPP and ET during the recovery period, respectively. The terms " continually degrade" in (c) and (d) refer to earthquake impact regions with GPP and ET, respectively, continually decreasing in the recovery period. "*" in (a) and (b) means the trend is statistically significant ($P < 0.10$).

largely attributable to the reduction in ET. As vegetation recovered, the WY fraction (the ratio of WY to precipitation) gradually decreased. For instance, in 2013, under precipitation conditions similar to 2010, the WY fraction was notably lower (0.46 versus 0.63) (Fig. 6a). During 2014–2017, despite significant variability in precipitation, the difference between the maximum variation in precipitation and WY was only 59.6 mm (40 % of precipitation variation) (Fig. 6a), indicating a reduced sensitivity of WY to precipitation changes. Spatially, areas with the greatest WY increase during the earthquake disturbance period corresponded closely to those experiencing the largest ET decreases (Fig. 6b), even though precipitation increased in these regions (Fig. S4). Similarly, during the recovery period, overall WY decreased due to rising ET (Fig. 6c), despite increased precipitation in the eastern part of the study area (Fig. S4), These patterns indicated that ET changes, rather than precipitation variations predominantly influenced WY changes in these regions.

3.3. Attributions of vegetation impacts to the earthquake and human intervention based on CCW and CIA

The earthquake had considerable negative impacts on NDVI, GPP, and ET, as evidenced in the CIA and CCW simulations (Fig. 7, S5). In a hypothetical scenario where only climatic factors were considered (excluding the earthquake), NDVI was projected to increase slightly by 0.01 (1.5 %), while GPP and ET were expected to decrease by 53.6 g C/ m^{-2}(−|-) (3.7 %) and 51.7 mm (11.2 %), respectively (Fig. 7). Comparing this counterfactual scenario with the actual outcomes reveals that the earthquake and its subsequent effects led to reductions in NDVI, GPP, and ET by 0.07 (11.2 %), 179.9 g C/m^{-2}(−|-) (12.5 %), and 56.3 mm (12.2 %), respectively (Fig. 7, S5). As a result, earthquake induced an increase in WY by 15.2 % compared to mean annual WY during 2001–2007. These changes account for 116.7 %, 77.0 %, 52.1 % and 26.4 % of the observed alterations in NDVI, GPP, ET, WY during the disturbance period, respectively.

Human intervention significantly contributed to the restoration of vegetation cover and eco-hydrological function (Fig. 6). In the absence of earthquake disturbances, climatic factors were expected to cause increases in NDVI, GPP, and ET after 2010, at rates of 0.007 per year ($P = 0.01$), 20.3 gC m^{-2} per year ($P < 0.10$), and 9.3 mm per year ($P < 0.10$), respectively (Fig. 7, S5). However, in the actual scenario, NDVI, GPP, and ET recovery rates accelerated to 0.012 per year ($P < 0.01$), 34.5 gC m^{-2} per year ($P < 0.05$), and 13.3 mm per year ($P < 0.10$), respectively

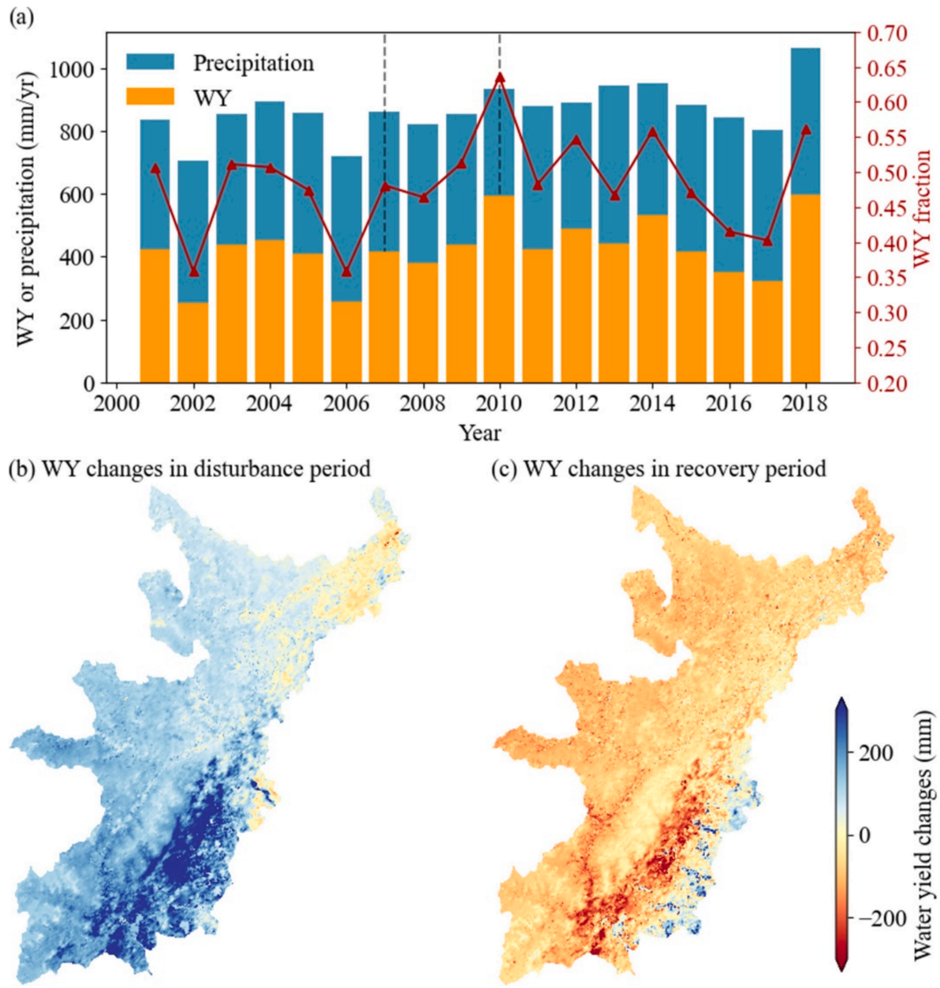

Fig. 6. Earthquake-induced spatial and temporal changes in water yield (WY). Annual WY, total precipitation and WY fraction (the ratio of WY to total precipitation) in the earthquake impact area during 2001–2018 (a), and spatial distributions of WY changes during 2007–2010 (b) and 2010–2018 (c).

(Fig. 7). Meanwhile, WY decreased with an insignificant rate of −9.9 mm per year (P = 0.47). This acceleration suggests that human intervention enhanced the recovery of NDVI, GPP, and ET by 0.005 per year, 15.2 gC m^{-2} per year, and 4.0 mm per year, respectively, contributing to 41.7 %, 41.2 %, and 30.1 % of the post-2010 recovery in NDVI, GPP, and ET, with climatic factors accounting for the remainder. As a result, human intervention was responsible for 38.9 % to the changes in WY during the recovery period.

Spatially, the earthquake's impact on GPP was most pronounced in mountainous areas near the epicenter, with contributions exceeding 75 % in most affected areas (Fig. 8), while its influences on ET and WY were less significant in high-altitude regions (Fig. 8). During the recovery period, areas significantly impacted by human intervention (contributing more than 75 %) were much smaller compared to those heavily affected by the earthquake (Fig. 8). County-level analysis revealed higher human intervention contribution rates to changes in GPP, ET, and WY in five densely populated, economically developed counties in the southeast, with Wenchuan County as an exception due to its proximity to the epicenter (Fig. 9). Strong correlations (0.76–0.87; Fig. 9f) were observed between these contribution rates and population and Gross Domestic Product density, providing supporting evidence for the role of human intervention in ecosystem function recovery. This spatial analysis, integrated with socio-economic contexts, offers valuable insights into the complex dynamics of post-earthquake ecological restoration.

4. Discussion

4.1. Significant disturbances in vegetation from the earthquake

Using remote sensing and model-based simulations, our study reveals that the 2008 Wenchuan earthquake caused significant disturbances in both vegetation structure and function. We established a spatial-resolved causal link between seismic activity and changes in vegetation cover and function that was previously unexplored. Our findings indicated that the earthquake was the primary catalyst for the observed changes in vegetation during the seismic event, as well as the predominant influence on the reductions in GPP and ET. Moreover, the reductions in ET have profound implications on the local hydrology, as ET is a key component of the water balance. The decline in ET induced an increase in water yield, as less water was lost to the atmosphere through transpiration and evaporation. This change in water yield can lead to higher soil moisture, increased surface runoff, and altered subsurface flow patterns (Lian et al., 2020).

The impacts of the earthquake on vegetation cover and function exhibited significant spatial heterogeneity, likely shaped by topographic and anthropogenic factors. In particular, the central Longmen Mountain area witnessed the most drastic vegetation disruptions (Fig. 4), pointing to landslides as a primary mechanism for earthquake-induced vegetation damage (Jiang et al., 2015; Jiao et al., 2014). Despite undergoing similarly intense seismic activity (Fig. 1a), the vegetation in the earthquake-impacted southern area suffered more extensive damage

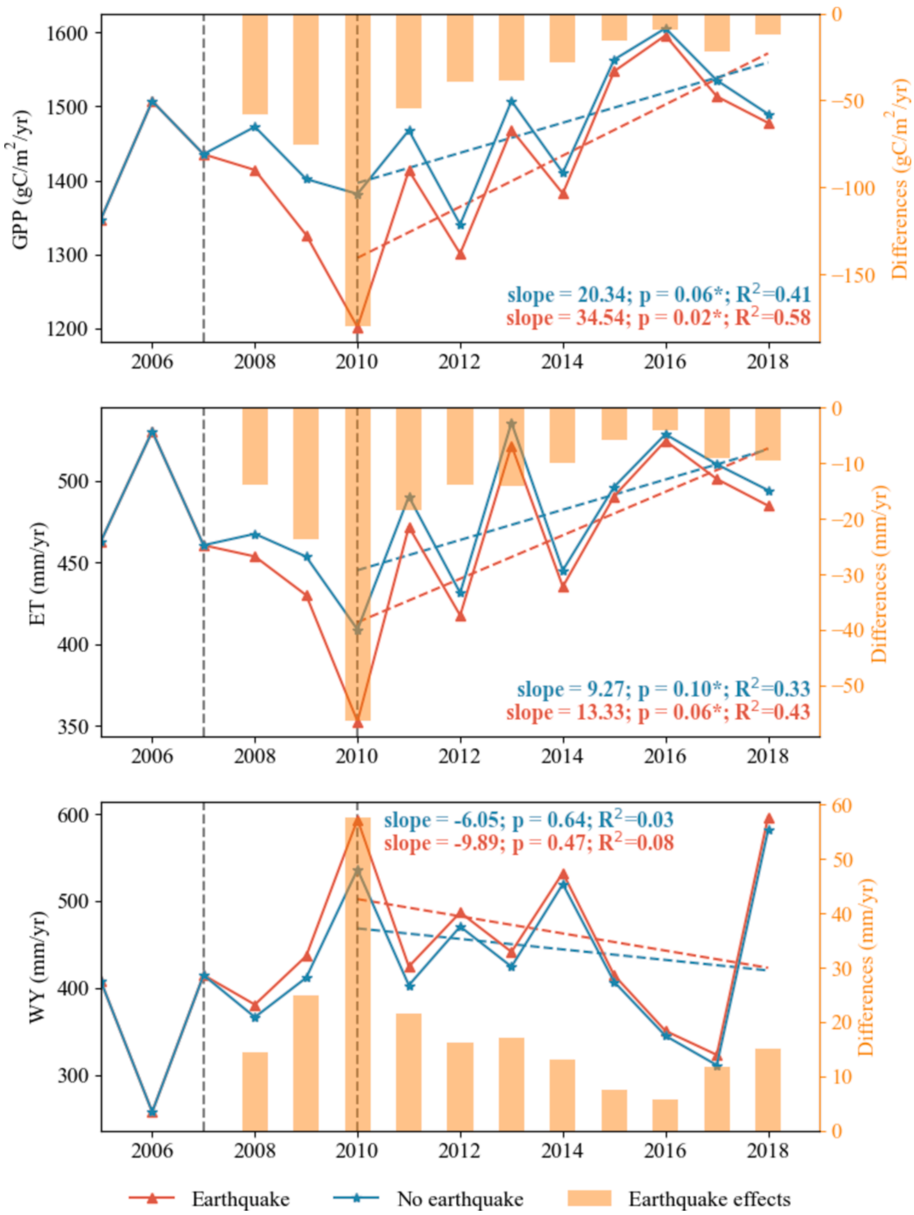

Fig. 7. CIA-based simulations in earthquake-induced GPP, ET and WY changes during earthquake disturbance and recovery periods. Actual scenario (blue line), CIA-based counter-factual scenario with no earthquake (red line), and the earthquake effects during disturbance period (yellow bar)). The differences in annual slopes of GPP, ET and WY between actual scenario and counter-factual scenario during the recovery period reflect the effects of human intervention. "*" denotes statistically significant trend at $P < 0.10$.

than the northern region (Fig. S3). This disparity likely arises from the mountainous terrain of the south, which may have experienced more severe landslides as a result. The reduction of ET in this region further implies significant hydrologic changes, including elevated soil moisture and increased surface and subsurface flows, which can contribute to landslide occurrences. Elevated soil moisture levels reduce soil cohesion, making slopes more susceptible to failure during subsequent rainfall events, thereby increasing the frequency and intensity of landslides following the earthquake.

In contrast, the earthquake-affected northern area, situated in a lower elevation valley, experienced less damage. Stable woodlands, including forests and shrublands, were the primary contributors to the changes in vegetation function during both the disturbance and recovery periods. This indicates that most woodland degradation from the earthquake was due to small-scale landslides that partially, but not completely, removed tree cover. Minimal canopy loss would reduce NDVI without necessarily changing the cover class, whereas more extensive canopy loss could lead to a shift in cover class, transforming forests into shrublands or grasslands. Consequently, the transition from "forest to shrubland" emerged as the dominant type of land conversion observed. The hydrologic implications in this northern area include a potential increase in base flow and streamflow stability due to reduced transpiration rates from the partially disturbed woodlands. These changes can affect downstream water availability and quality, influencing both ecological and human water use.

Post-earthquake human activities also played a crucial role in shaping vegetation cover change, particularly in the southeast plains, where a marked decrease in cropland coverage was noted from 2008 to 2010 (Fig. 3b). This reduction is likely linked to changes in human behavior following the earthquake (Cui et al., 2012; Xu et al., 2008). After the east Japan earthquake in 2011, it was also found that a large number of rice paddies were transformed into grasslands, due to restricted human activities in evacuation zones and areas of high radioactive contamination (Ishihara and Tadono, 2017). The seismic

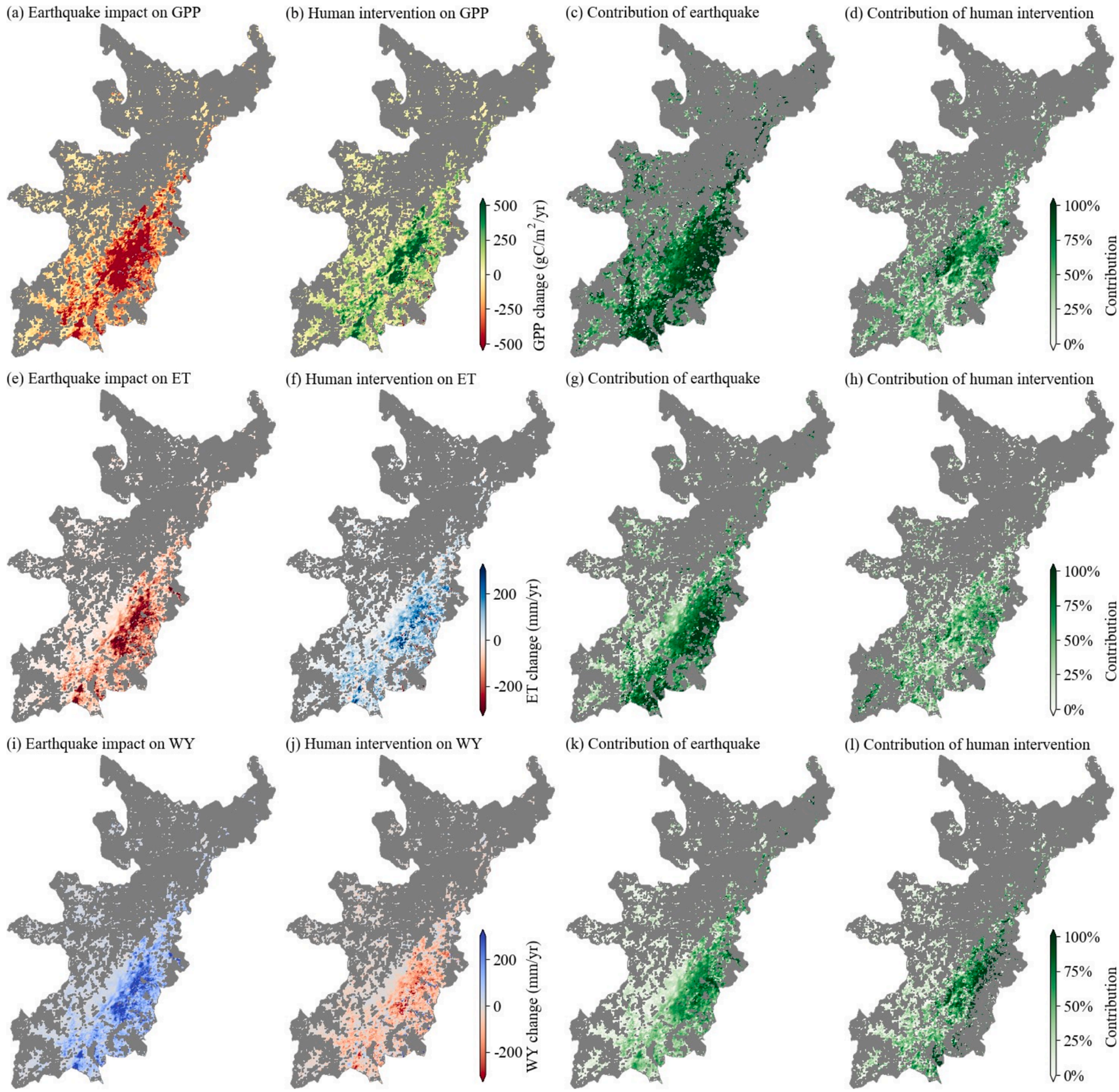

Fig. 8. Spatial patterns of impacts of direct earthquake during disturbance period (2007–2010) and human intervention during the recover period (2010–2018) on GPP (a-d), ET (e-h) and WY (i-l). For each row, the left two subfigures show the impact magnitude from earthquake and human intervention, and right two subfigures show the proportional contributions of earthquake and human intervention on the total changes of GPP, ET and WY during the disturbance period and recovery period, respectively.

event not only diminished the local agricultural workforce and damaged irrigation systems (Li et al., 2009) but also caused profound psychological distress among the residents (Ahmad et al., 2010). The socio-economic-psychological effects of the earthquake were multifaceted and profound. The loss of life and displacement of communities resulted in a significant reduction in the labor force available for agricultural activities, discouraging farming. The economic instability caused by the earthquake led to increased poverty and financial insecurity, compelling many residents to seek alternative livelihoods in urban areas (Thiri, 2017), further exacerbating the decline in farming activities. These combined factors may have reduced agricultural productivity and capacity, leading to a temporary but widespread abandonment of cropland. Moreover, the decline in agricultural activity likely reduced water extraction for irrigation, further influencing local water yield by allowing more water to remain in the hydrological system.

4.2. Roles of climatic and anthropogenic factors in the post-earthquake vegetation recovery

Our findings highlight the ability of landscape-scale vegetation cover and ecosystem carbon and water functions to recover quickly and effectively from severe seismic disturbances, which aligns with previous studies (Chen et al., 2022; Jiang et al., 2015; Jiao et al., 2014; Liu et al., 2017; Yunus et al., 2020). For instance, we observed that 70 % of the

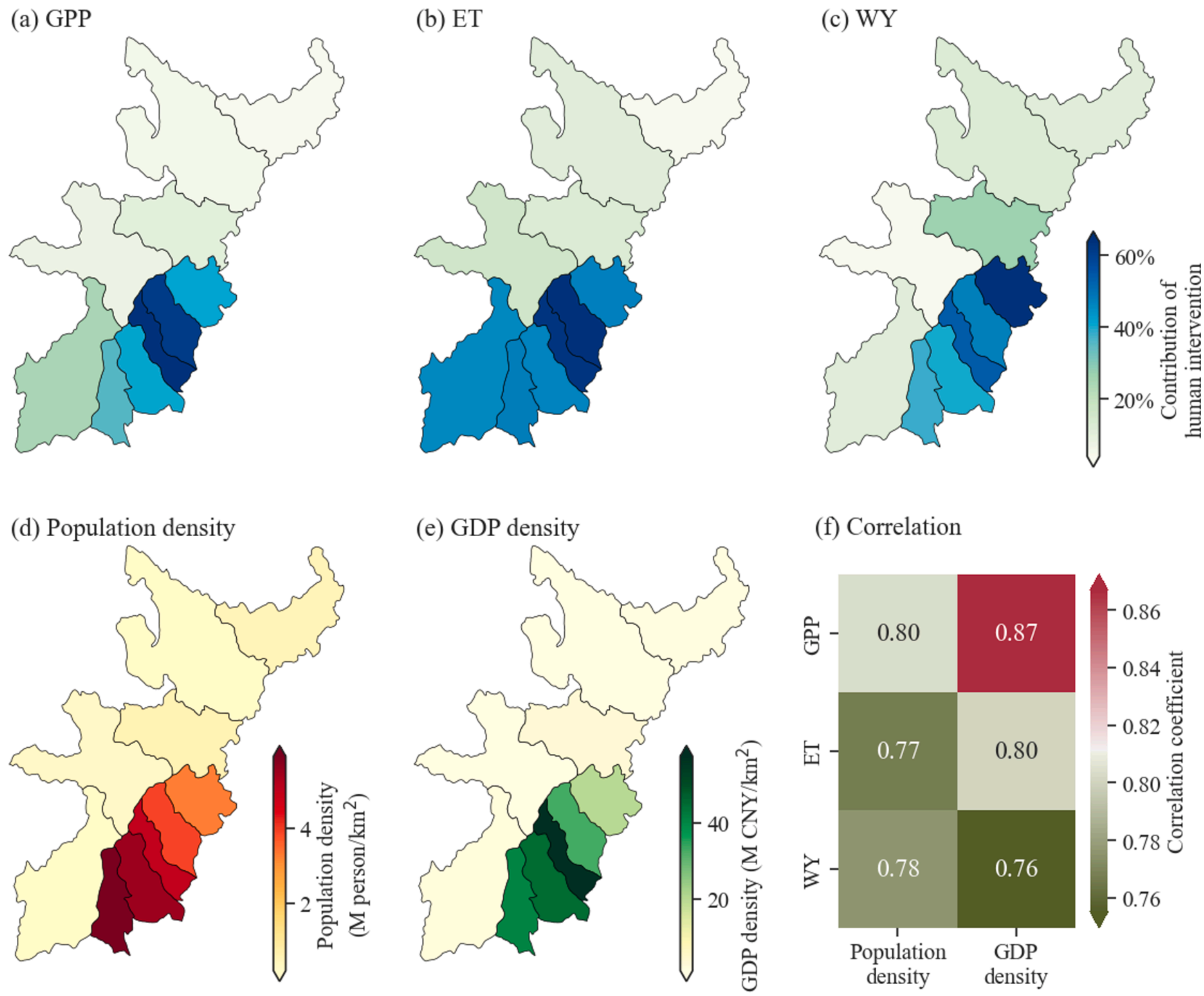

Fig. 9. Spatial patterns of the contribution of human interventions to GPP, ET and WY changes at county level during recovery period (a, b, c), along with the socio-economic backgrounds of county-level population density (d) and Gross Domestic Product (GDP) density (e) in 2022. (f) presents the county-level correlations between socio-economic backgrounds (population density and GDP density) and human intervention effects on GPP, ET and WY changes simulated by CCW.

damaged vegetated area returned to pre-earthquake levels by 2018, a decade post-earthquake. This is in line with Jiang et al. (2015), who noted a 41 % restoration by 2013, and Liu et al. (2017) who reported a 44.2 % recovery by 2016. Additionally, Jiao et al. (2014) documented a 68 % recovery within three years and complete restoration within eight to nine years. In the context of other earthquake events, the Jiujiu Peaks earthquake (1999) in Taiwan saw an 80 % recovery of impacted vegetation over two decades (Lin et al., 2023), while vegetation affected by the Chuetsu earthquake (2004) in Japan restored 85.5 % by 2021 (Xiang et al., 2023). However, these studies primarily focused on the recovery of vegetation cover, with less exploration into the recovery of eco-hydrological functions and did not delve into the underlying mechanisms of vegetation recovery nor into explicit causal analysis of the earthquake's effects.

Our study also examined the hydrological implications of vegetation recovery post-earthquake. The restoration of vegetation function plays a crucial role in stabilizing local water cycles (Wang et al., 2018). Specifically, GPP reflects the rate at which plants convert atmospheric carbon dioxide into biomass through photosynthesis, indicating the overall health and productivity of vegetation (Spielmann et al., 2019). ET, on the other hand, represents a significant component of the water cycle (Schlesinger and Jasechko, 2014). During the recovery period, the increase in ET rates led to a gradually enhanced regulation on WY. Recovering vegetation enhances soil structure and water retention capacity (Fan et al., 2022), promoting consistent soil moisture levels crucial for plant growth and soil stability (Gregory et al., 2006). Reestablished vegetation canopies intercepts rainfall, slowing down the rate at which water reaches the ground and thereby reducing the rate of flash flooding (Gardon et al., 2020). Furthermore, the roots of recovering vegetation binds the soil, enhancing slope stability and reducing the risk of landslides (Fan et al., 2022) This protective role of vegetation is particularly important in post-earthquake landscapes, where the risk of landslides and erosion is significantly heightened due to the initial loss of vegetation cover and soil disturbance.

Our study highlighted the relative contributions of climatic variability and human intervention on vegetation recovery post-earthquake. We found that climatic factors, particularly climatic conditions, and vegetation natural growth, were the primary drivers of recovery after the Wenchuan earthquake. In simulated scenarios with no earthquake influence, the earthquake-affected area still exhibited a significant upward trend in NDVI, suggesting that the recovery was possibly accelerated due to climate variability, other factors like CO_2 fertilization or continued regrowth of secondary forests (Zhu et al., 2016), which were independent from human-led initiatives such as grass and tree planting and conservation efforts. The spatial variability of climate also had a significant impact, with recovery rates across Longmen Mountain's eastern slope outpacing the western side (Fig. 5), possibly due to its warmer, more humid climate from the subtropical monsoon, which could aid faster forest recovery. Conversely, the cooler, drier conditions of the western side and the mountain top impeded recovery (Wu et al., 2008). Climatic factors accounted for approximately 23 %-56 % of the changes in GPP and ET during the recovery period (Fig. 6), indicating their substantial role in restoring vegetation function.

Human intervention significantly influenced the restoration of vegetation function, accounting for 30.1 % and 41.7 % of the recovery in GPP and ET, respectively (Fig. 6). Notably, artificial restoration efforts in the aftermath of the 2015 Nepal Gorkha earthquake contributed to vegetation recovery, though they were only about one-tenth as effective as natural factors (Pandey et al., 2022). In response to the Wenchuan earthquake, China implemented the "Special Plan for Ecological Restoration after the Wenchuan Earthquake," advocating a balanced approach that prioritizes natural recovery while incorporating artificial measures (State Council of China, 2008). This led to substantial reforestation initiatives, particularly noticeable in transforming grasslands or croplands into woodlands. In heavily affected areas like Aba Prefecture, significant efforts were made to increase forest coverage, with new forests spanning 240 km^2 established and an additional 950 km^2 of forests conserved in 2008 and 2009 (the National Bureau of Forestry and Grassland of China, 2020). Further, the resumption of agricultural activities as communities were rebuilt and farmers returned to their lands contributed to the gradual recovery of cropland vegetation, illustrating the multifaceted nature of anthropogenic contributions to post-earthquake ecological restoration. These human interventions not only facilitated vegetation recovery but also played a critical role in stabilizing local hydrological cycles by increasing ET, improving infiltration rates, and reducing surface runoff.

4.3. Uncertainties and implications

In this study, we tracked the recovery of vegetation cover and functions by five indicators: land cover, NDVI, GPP, ET and WY. However, it is worthy to acknowledge that these metrics do not encapsulate the full spectrum of vegetation structure and function recovery. A recent species-level study (Allen et al., 2020) indicated that factors such as soil-available phosphorus, tree diameter, and distance from the earthquake epicenter play critical roles in tree survival and growth post-disaster. Our model simulations at the ecosystem level, while informative, may not fully capture the actual state of fine-scale (or species level) vegetation recovery, especially in regarding to tree heath and survival. Therefore, future studies should expand scope to include a wider range of ecological metrics and observational data from stand to ecosystem scales to better account for the nuanced factors affecting vegetation health and resilience in earthquake-affected areas. In this study, we used MODIS land cover with a 500 m resolution, which, despite its utility, suffers from classification errors and has limitations in detecting fine-scale details of landslides commonly triggered by earthquakes. The lack of high-resolution, continuous land cover data specific to our study area posed a challenge. We used NDVI as an indirect measure to detect finer-scale land cover changes, but future research would benefit from employing higher-resolution data for more precise modeling and analysis. We adopted WY as a hydrological response indicator. However, the relationship between WY and downstream water resources, including the non-stationarity effects of soil storage, recharge and outflow in the context of vegetation disturbance and post recovery, was not addressed in our study and requires further investigation in the future.

We conducted spatial resolved CIA-based on certain necessary assumptions, which may introduce some potential uncertainties. For instance, we used pixels with minimal NDVI changes during the earthquake as control samples to estimate what the NDVI time series would have looked like for earthquake-affected pixels under normal conditions. This approach assumes these control pixels remained in a stable condition, unaffected by other factors other than climate. However, it is challenging to guarantee the complete absence of such influences. Future ground-based surveys and high-resolution remote sensing (e.g., drone-based mapping and lidar scanning) may help to further evaluate our findings. Despite the aforementioned limitations, our study presents a comprehensive framework for quantifying the immediate and subsequent effects of earthquakes on vegetation structure and eco-hydrological functions. The methodologies employed, such as before-after comparisons, neighborhood pair comparisons, and spatially resolved CIA-based theoretical simulations, can be readily applied to other regions and other types of disturbances, such as wildfires and deforestation.

5. Conclusion

This study utilized remote sensing techniques and model-based simulations to assess the impact and subsequent recovery of vegetation cover and eco-hydrological function following the Wenchuan earthquake. We found that the vegetation disturbance triggered by the earthquake persisted for three years from 2008 to 2010, resulting in significant disruptions to vegetation cover over 12 % of the study area and a reduction in GPP by 7.5 % and in ET by 14.7 %. During this period, the affected regions experienced a significant increase in water yield (WY), primarily due to a decrease in evapotranspiration (ET). During the recovery period from 2010 to 2018, vegetation function in terms of GPP and ET showed rapid recovery, but they did not fully reach the levels projected in a hypothetical scenario without the earthquake. Our spatial-resolved CIA analysis indicated that the recovery process following the earthquake was primarily driven by climatic factors. Human intervention also played a crucial role in this recovery, contributing to 30.1 %, 41.7 % and 38.9 % of the improvements in GPP, ET and WY, respectively. Our findings highlight the vulnerability and resilience of mountain ecosystems in response to severe disturbance, emphasizing the critical roles played by both climatic factors and human intervention in the restoration of vegetation structure and function. These insights are vital for understanding post-earthquake dynamics and informing management and policy decisions for future natural disaster responses.

Author contributions

J.Z. and Y.Z. initiated and conceptualized the study; J.Z. and Y.Z. designed the experiments, gathered data, wrote the codes, and carried out the analysis; Y.Z. provided the CCW model and parameters; J.Z. and Y.Z. contributed to the interpretation of the results and wrote the paper, with all authors contributing to the commenting, reviewing, and editing of the paper.

Fundings

No official funding was received to directly support this work.

CRediT authorship contribution statement

Jiehao Zhang: Writing – review & editing, Writing – original draft, Visualization, Validation, Software, Methodology, Investigation, Formal analysis, Data curation, Conceptualization. **Yulong Zhang:** Writing – review & editing, Writing – original draft, Supervision, Software, Investigation, Conceptualization. **Matthew P. Dannenberg:** Writing – review & editing, Methodology. **Qinfeng Guo:** Writing – review & editing. **Jeff W. Atkins:** . **Wenhong Li:** Writing – review & editing. **Ge Sun:** Writing – review & editing, Writing – original draft, Funding acquisition.

Declaration of competing interest

The authors declare that they have no known competing financial interests or personal relationships that could have appeared to influence the work reported in this paper.

Acknowledgements

We acknowledge the public data provided by NASA MODIS, TerraClimate, and the Water Resources Bulletin of the Yangtze River Basin and Southwest Rivers, and the R package CausalImpact provided by Dr. Kay H. Brodersen. The research was primarily conducted at the Department of Land Resources Administration of China University of Geosciences (Wuhan), with additional support from the Remote Sensing and Ecological Modeling group in the Department of Geography at the University of North Carolina at Chapel Hill, USA. Y.Z. is partially supported by USDA Forest Service and Duke University. This research serves as a tribute to those who perished in the Wenchuan earthquake, as well as an expression of reverence for the formidable power of nature.

Appendix A. Supplementary data

Supplementary data to this article can be found online at https://doi.org/10.1016/j.jhydrol.2024.132595.

Data availability

Data will be made available on request.

References

Abatzoglou, J.T., Dobrowski, S.Z., Parks, S.A., Hegewisch, K.C., 2018. TerraClimate, a high-resolution global dataset of monthly climate and climatic water balance from 1958-2015. Sci. Data 5, 170191. https://doi.org/10.1038/sdata.2017.191.

Ahmad, S., Feder, A., Lee, E.J., Wang, Y., Southwick, S.M., Schlackman, E., Buchholz, K., Alonso, A., Charney, D.S., 2010. Earthquake impact in a remote South Asian population: psychosocial factors and posttraumatic symptoms. J. Trauma. Stress 23, 408–412. https://doi.org/10.1002/jts.20535.

Allen, R.B., MacKenzie, D.I., Bellingham, P.J., Wiser, S.K., Arnst, E.A., Coomes, D.A., Hurst, J.M., 2020. Tree survival and growth responses in the aftermath of a strong earthquake. J. Ecol. 108, 107–121. https://doi.org/10.1111/1365-2745.13238.

Bao, W., 2008. Ecological degradation and restoration and reconstruction countermeasures for severe calamity regions in wenchuan earthquake in sichuan. Bull. Chin. Acad. Sci. Chin. 4, 324–329. https://doi.org/10.16418/j.issn.1000-3045.2008.04.005.

Bao, W., Pang, X., 2008. Ecological degradation in the wenchuan earthquake seriously affected region in Sichuan, China. Chin. J. Appl. Environ. Biol. Chin. 14, 441–444.

Brodersen, K.H., Gallusser, F., Koehler, J., Remy, N., Scott, S.L., 2015. Inferring causal impact using bayesian structural time-series models. Appl. Stat Ann. https://doi.org/10.1214/14-AOAS788.

Chen, M., Tang, C., Wang, X., Xiong, J., Shi, Q., Zhang, X., Li, M., Luo, Y., Tie, Y., Feng, Q., 2021. Temporal and spatial differentiation in the surface recovery of post-seismic landslides in wenchuan earthquake-affected areas. Ecol. Inform. 64, 101356. https://doi.org/10.1016/j.ecoinf.2021.101356.

Chen, M., Tang, C., Li, M., Xiong, J., Luo, Y., Shi, Q., Zhang, X., Tie, Y., Feng, Q., 2022. Changes of surface recovery at coseismic landslides and their driving factors in the Wenchuan earthquake-affected area. CATENA 210, 105871. https://doi.org/10.1016/j.catena.2021.105871.

Crowley, M.A., Cardille, J.A., 2020. Remote sensing's recent and future contributions to landscape ecology. Curr. Landsc. Ecol. Rep. 5, 45–57. https://doi.org/10.1007/s40823-020-00054-9.

Cui, P., Lin, Y., Chen, C., 2012. Destruction of vegetation due to geo-hazards and its environmental impacts in the wenchuan earthquake areas. Ecol. Eng. 44, 61–69. https://doi.org/10.1016/j.ecoleng.2012.03.012.

Dannenberg, M.P., Smith, W.K., Zhang, Y., Song, C., Huntzinger, D.N., Moore, D.J.P., 2021. Large-scale reductions in terrestrial carbon uptake following central pacific El Niño. Geophys. Res. Lett. 48, e2020GL092367. https://doi.org/10.1029/2020GL092367.

Deng, X., Jiang, Q., Ge, Q., Yang, L., 2010. Impacts of the wenchuan earthquake on the giant panda nature reserves in China. J. Mt. Sci. 7, 197–206. https://doi.org/10.1007/s11629-010-1073-8.

Duan, Y., Di, B., Ustin, S.L., Xu, C., Xie, Q., Wu, S., Li, J., Zhang, R., 2021. Changes in ecosystem services in a montane landscape impacted by major earthquakes: A case study in wenchuan earthquake-affected area, China. Ecol. Indic. 126, 107683. https://doi.org/10.1016/j.ecolind.2021.107683.

Fan, X., Domènech, G., Scaringi, G., Huang, R., Xu, Q., Hales, T.C., Dai, L., Yang, Q., Francis, O., 2018. Spatio-temporal evolution of mass wasting after the 2008 mw 7.9 wenchuan earthquake revealed by a detailed multi-temporal inventory. Landslides 15, 2325–2341. https://doi.org/10.1007/S10346-018-1054-5/FIGURES/10.

Fan, L., Lehmann, P., Zheng, C., Or, D., 2022. Vegetation-promoted soil structure inhibits hydrologic landslide triggering and alters carbon fluxes. Geophys. Res. Lett. 49, e2022GL100389. https://doi.org/10.1029/2022GL100389.

Gan, B., Yang, X., Zhang, W., Zhou, J., 2019. Temporal and spatial evolution of vegetation coverage in the Mianyuan river basin influenced by strong earthquake disturbance. Sci. Rep. 9, 16762. https://doi.org/10.1038/s41598-019-53264-5.

Gardon, F.R., de Toledo, R.M., Brentan, B.M., dos Santos, R.F., 2020. Rainfall interception and plant community in young forest restorations. Ecol. Indic. 109, 105779. https://doi.org/10.1016/j.ecolind.2019.105779.

Garwood, N.C., Janos, D.P., Brokaw, N., 1979. Earthquake-caused landslides: a major disturbance to tropical forests. Science 205, 997–999. https://doi.org/10.1126/science.205.4410.997.

Gregory, J.H., Dukes, M.D., Jones, P.H., Miller, G.L., 2006. Effect of urban soil compaction on infiltration rate. J. Soil Water Conserv. 61, 117–124.

Han, J., Yang, Y., Roderick, M.L., McVicar, T.R., Yang, D., Zhang, S., Beck, H.E., 2020. Assessing the steady-state assumption in water balance calculation across global catchments. Water Resources Research 56 (7), e2020WR027392.

Ishihara, M., Tadono, T., 2017. Land cover changes induced by the great east Japan earthquake in 2011. Sci. Rep. 7, 45769. https://doi.org/10.1038/srep45769.

Jiang, W.-G., Jia, K., Wu, J.-J., Tang, Z.-H., Wang, W.-J., Liu, X.-F., 2015. Evaluating the vegetation recovery in the damage area of wenchuan earthquake using MODIS data. Remote Sens. 7, 8757–8778. https://doi.org/10.3390/rs70708757.

Jiao, Q., Zhang, B., Liu, L., Li, Z., Yue, Y., Hu, Y., 2014. Assessment of spatio-temporal variations in vegetation recovery after the wenchuan earthquake using landsat data. Nat. Hazards 70, 1309–1326. https://doi.org/10.1007/s11069-013-0875-8.

Jönsson, P., Eklundh, L., 2004. TIMESAT - a program for analyzing time-series of satellite sensor data. Comput. Geosci. 30, 833–845. https://doi.org/10.1016/j.cageo.2004.05.006.

Khan, S.F., Kamp, U., Owen, L.A., 2013. Documenting five years of landsliding after the 2005 Kashmir earthquake, using repeat photography. Geomorphology 197, 45–55. https://doi.org/10.1016/j.geomorph.2013.04.033.

Li, C., Wang, M., Liu, K., 2018. A decadal evolution of landslides and debris flows after the wenchuan earthquake. Geomorphology 323, 1–12. https://doi.org/10.1016/J.GEOMORPH.2018.09.010.

Li, Q., Zhang, F., Du, X., Wu, B., Zhang, L., Wei, Y., 2009. Grain losses in main disaster area caused by wenchuan earthquake. J. Remote Sens. 13, 928–939.

Lian, X., Piao, S., Li, L.Z.X., Li, Y., Huntingford, C., Ciais, P., Cescatti, A., Janssens, I.A., Peñuelas, J., Buermann, W., Chen, A., Li, X., Myneni, R.B., Wang, X., Wang, Y., Yang, Y., Zeng, Z., Zhang, Y., McVicar, T.R., 2020. Summer soil drying exacerbated by earlier spring greening of northern vegetation. Sci. Adv. 6, eaax0255. https://doi.org/10.1126/sciadv.aax0255.

Lin, W.-T., Huang, P.-H., Chou, T.-Y., 2023. Mechanisms of vegetation restoration at landslides caused by a catastrophic earthquake in Central Taiwan. Ecol. Eng. 190, 106929. https://doi.org/10.1016/j.ecoleng.2023.106929.

Lin, C.W., Shieh, C.L., Yuan, B.D., Shieh, Y.C., Liu, S.H., Lee, S.Y., 2004. Impact of chi-chi earthquake on the occurrence of landslides and debris flows: Example from the chenyulan river watershed, Nantou, Taiwan. Eng. Geol. 71, 49–61. https://doi.org/10.1016/S0013-7952(03)00125-X.

Liu, X., Jiang, W., Li, J., Wang, W., 2017. Evaluation of the vegetation coverage resilience in areas damaged by the wenchuan earthquake based on MODIS-EVI data. Sensors 17, 259. https://doi.org/10.3390/s17020259.

Logan, T.M., Aven, T., Guikema, S.D., Flage, R., 2022. Risk science offers an integrated approach to resilience. Nat. Sustain. 5, 741–748. https://doi.org/10.1038/s41893-022-00893-w.

Long, D., Yang, Y., Wada, Y., Hong, Y., Liang, W., Chen, Y., Chen, L., 2015. Deriving scaling factors using a global hydrological model to restore GRACE total water storage changes for China's Yangtze River Basin. Remote Sensing of Environment 168, 177–193.

Ma, C., Wang, Y., Hu, K., Du, C., Yang, W., 2017. Rainfall intensity–duration threshold and erosion competence of debris flows in four areas affected by the 2008 Wenchuan earthquake. Geomorphology 282, 85–95. https://doi.org/10.1016/j.geomorph.2017.01.012.

Marc, O., Hovius, N., Meunier, P., Uchida, T., Hayashi, S., 2015. Transient changes of landslide rates after earthquakes. Geology 43, 883–886. https://doi.org/10.1130/G36961.1.

Ouyang, Z., Xu, W., Wang, X., Wang, W., Dong, R., Zheng, H., 2008. Impact assessment of wenchuan earthquake on ecosystems. Acta Ecol. Sin. Chin. 28, 5801–5809.

Pandey, H.P., Gnyawali, K., Dahal, K., Pokhrel, N.P., Maraseni, T.N., 2022. Vegetation loss and recovery analysis from the 2015 Gorkha earthquake (7.8 Mw) triggered landslides. Land Use Policy 119, 106185. https://doi.org/10.1016/j.landusepol.2022.106185.

Pastorello, G., Trotta, C., Canfora, E., Chu, H., Christianson, D., Cheah, Y.W., Poindexter, C., Chen, J., Elbashandy, A., Humphrey, M., Isaac, P., Polidori, D., Ribeca, A., van Ingen, C., Zhang, L., Amiro, B., Ammann, C., Arain, M.A., Ardö, J., Arkebauer, T., Arndt, S.K., Arriga, N., Aubinet, M., Aurela, M., Baldocchi, D., Barr, A., Beamesderfer, E., Marchesini, L.B., Bergeron, O., Beringer, J., Bernhofer, C., Berveiller, D., Billesbach, D., Black, T.A., Blanken, P.D., Bohrer, G., Boike, J., Bolstad, P.V., Bonal, D., Bonnefond, J.M., Bowling, D.R., Bracho, R., Brodeur, J., Brümmer, C., Buchmann, N., Burban, B., Burns, S.P., Buysse, P., Cale, P., Cavagna, M., Cellier, P., Chen, S., Chini, I., Christensen, T.R., Cleverly, J., Collalti, A., Consalvo, C., Cook, B.D., Cook, D., Coursolle, C., Cremonese, E., Curtis, P.S., D'Andrea, E., da Rocha, H., Dai, X., Davis, K.J., De Cinti, B., de Grandcourt, A., De Ligne, A., De Oliveira, R.C., Delpierre, N., Desai, A.R., Di Bella, C. M., di Tommasi, P., Dolman, H., Domingo, F., Dong, G., Dore, S., Duce, P., Dufrêne, E., Dunn, A., Dušek, J., Eamus, D., Eichelmann, U., ElKhidir, H.A.M., Eugster, W., Ewenz, C.M., Ewers, B., Famulari, D., Fares, S., Feigenwinter, I., Feitz, A., Fensholt, R., Filippa, G., Fischer, M., Frank, J., Galvagno, M., Gharun, M., Gianelle, D., Gielen, B., Gioli, B., Gitelson, A., Goded, I., Goeckede, M., Goldstein, A. H., Gough, C.M., Goulden, M.L., Graf, A., Griebel, A., Gruening, C., Grünwald, T., Hammerle, A., Han, S., Han, X., Hansen, B.U., Hanson, C., Hatakka, J., He, Y., Hehn, M., Heinesch, B., Hinko-Najera, N., Hörtnagl, L., Hutley, L., Ibrom, A., Ikawa, H., Jackowicz-Korczynski, M., Janouš, D., Jans, W., Jassal, R., Jiang, S., Kato, T., Khomik, M., Klatt, J., Knohl, A., Knox, S., Kobayashi, H., Koerber, G., Kolle, O., Kosugi, Y., Kotani, A., Kowalski, A., Kruijt, B., Kurbatova, J., Kutsch, W.L., Kwon, H., Launiainen, S., Laurila, T., Law, B., Leuning, R., Li, Y., Liddell, M., Limousin, J.M., Lion, M., Liska, A.J., Lohila, A., López-Ballesteros, A., López-Blanco, E., Loubet, B., Loustau, D., Lucas-Moffat, A., Lüers, J., Ma, S., Macfarlane, C., Magliulo, V., Maier, R., Mammarella, I., Manca, G., Marcolla, B., Margolis, H.A., Marras, S., Massman, W., Mastepanov, M., Matamala, R., Matthes, J.H., Mazzenga, F., McCaughey, H., McHugh, I., McMillan, A.M.S., Merbold, L., Meyer, W., Meyers, T., Miller, S.D., Minerbi, S., Moderow, U., Monson, R.K., Montagnani, L., Moore, C.E., Moors, E., Moreaux, V., Moureaux, C., Munger, J.W., Nakai, T., Neirynck, J., Nesic, Z., Nicolini, G., Noormets, A., Northwood, M., Nosetto, M., Nouvellon, Y., Novick, K., Oechel, W., Olesen, J.E., Ourcival, J.M., Papuga, S.A., Parmentier, F.J., Paul-Limoges, E., Pavelka, M., Peichl, M., Pendall, E., Phillips, R.P., Pilegaard, K., Pirk, N., Posse, G., Powell, T., Prasse, H., Prober, S.M., Rambal, S., Rannik, Ü., Raz-Yaseef, N., Reed, D., de Dios, V.R., Restrepo-Coupe, N., Reverter, B.R., Roland, M., Sabbatini, S., Sachs, T., Saleska, S.R., Sánchez-Cañete, E. P., Sanchez-Mejia, Z.M., Schmid, H.P., Schmidt, M., Schneider, K., Schrader, F., Schroder, I., Scott, R.L., Sedlák, P., Serrano-Ortíz, P., Shao, C., Shi, P., Shironya, I., Siebicke, L., Šigut, L., Silberstein, R., Sirca, C., Spano, D., Steinbrecher, R., Stevens, R.M., Sturtevant, C., Suyker, A., Tagesson, T., Takanashi, S., Tang, Y., Tapper, N., Thom, J., Tiedemann, F., Tomassucci, M., Tuovinen, J.P., Urbanski, S., Valentini, R., van der Molen, M., van Gorsel, E., van Huissteden, K., Varlagin, A., Verfaillie, J., Vesala, T., Vincke, C., Vitale, D., Vygodskaya, N., Walker, J.P., Walter-Shea, E., Wang, H., Weber, R., Westermann, S., Wille, C., Wofsy, S., Wohlfahrt, G., Wolf, S., Woodgate, W., Li, Y., Zampedri, R., Zhang, J., Zhou, G., Zona, D., Agarwal, D., Biraud, S., Torn, M., Papale, D., 2020. The FLUXNET2015 dataset and the ONEFlux processing pipeline for eddy covariance data. Sci. Data 7, 225. https://doi.org/10.1038/s41597-020-0534-3.

Peng, B., Fu, Y., 2018. Change characteristic of landscape ecological pattern in Lushan county by disaster reconstruction disturbance. Ecol. Sci. Chin. 37, 178–187. https://doi.org/10.14108/j.cnki.1008-8873.2018.04.022.

Peng, Y., Wang, Y., Fu, B., Ma, F., 2013. Spatial distribution of carbon storage function and seismic damage in wenchuan earthquake stricken areas. Acta Ecol. Sin. Chin. 33, 798–808.

Running, S.W., Thornton, P.E., Nemani, R., Glassy, J.M., 2000. Global terrestrial gross and net primary productivity from the earth observing system. Springer, New York, pp. 44–57.

Schlesinger, W.H., Jasechko, S., 2014. Transpiration in the global water cycle. Agric. for. Meteorol. 189–190, 115–117. https://doi.org/10.1016/j.agrformet.2014.01.011.

Scholes, R., Montanarella, L., Brainich, A., Barger, N., ten Brink, B., Cantele, M., Erasmus, B., Fisher, J., Gardner, T., Holland, T.G., et al., 2018. Summary for policymakers of the assessment report on land degradation and restoration of the intergovernmental science-policy platform on biodiversity and ecosystem services. IPBES Secretariat Intergovernmental Science-Policy Platform on Biodiversity and Ecosystem Services, Bonn, Germany.

Seidl, R., Turner, M.G., 2022. Post-disturbance reorganization of forest ecosystems in a changing world. Proc. Natl. Acad. Sci. 119, e2202190119. https://doi.org/10.1073/pnas.2202190119.

Spielmann, F.M., Wohlfahrt, G., Hammerle, A., Kitz, F., Migliavacca, M., Alberti, G., Ibrom, A., El-Madany, T.S., Gerdel, K., Moreno, G., Kolle, O., Karl, T., Peressotti, A., Vedove, G.D., 2019. Gross primary productivity of four european ecosystems constrained by joint CO2 and COS flux measurements. Geophys. Res. Lett. 46, 5284–5293. https://doi.org/10.1029/2019GL082006.

State Council of China, 2008. Wenchuan earthquake recovery and reconstruction of ecological restoration special planning.

Sulla-Menashe, D., Gray, J.M., Abercrombie, S.P., Friedl, M.A., 2019. Hierarchical mapping of annual global land cover 2001 to present: The MODIS collection 6 land cover product. Remote Sens. Environ. 222, 183–194. https://doi.org/10.1016/j.rse.2018.12.013.

Tang, C., Van Westen, C.J., Tanyas, H., Jetten, V.G., 2016. Analysing post-earthquake landslide activity using multi-temporal landslide inventories near the epicentral area of the 2008 wenchuan earthquake. Nat. Hazards Earth Syst. Sci. 16, 2641–2655. https://doi.org/10.5194/NHESS-16-2641-2016.

the National Bureau of Forestry and Grassland of China, 2020. China forest resources report (2014-2018). China Forestry Press, Beijing.

Thiri, M.A., 2017. Social vulnerability and environmental migration: The case of Miyagi Prefecture after the Great East Japan Earthquake. Int. J. Disaster Risk Reduct. 25, 212–226. https://doi.org/10.1016/j.ijdrr.2017.08.002.

UNCRD, 2009. Report on the 2008 great sichuan earthquake. United Nations Centre for Regional Development (UNCRD).

Wang, Q., Wang, Z., Yong, Z., Zhao, K., Xiong, J., Du, X., Zhao, Y., 2022. Vegetation recovery trends under dual dominance of climate change and anthropogenic factors in the severely damaged areas of the Wenchuan earthquake. J. Mt. Sci. 19, 3131–3147. https://doi.org/10.1007/s11629-022-7553-9.

Wang, L., Wei, X., Bishop, K., Reeves, A.D., Ursino, N., Winkler, R., 2018. Vegetation changes and water cycle in a changing environment. Hydrol. Earth Syst. Sci. 22, 1731–1734. https://doi.org/10.5194/hess-22-1731-2018.

Wu, L., Lu, T., Luo, P., Zhu, D., 2008. A review of the impacts of earthquake on mountain ecosystems: taking 5.12 wenchuan earthquake as an example. Acta Ecol. Sin. Chin. 28, 5810–5819.

Xiang, Z., Dou, J., Yunus, A.P., Zhang, L., Wang, X., Luo, W., 2023. Vegetation-landslide nexus and topographic changes post the 2004 Mw 6.6 Chuetsu earthquake. CATENA 223, 106946. https://doi.org/10.1016/j.catena.2023.106946.

Xu, X., Jiang, D., Zhuang, D., Qiu, D., 2008. Assessment about the impact of wenchuan earthquake on ecological environment. Acta Ecol. Sin. Chin. 28, 5899–5908.

Yunus, A.P., Fan, X., Tang, X., Jie, D., Xu, Q., Huang, R., 2020. Decadal vegetation succession from MODIS reveals the spatio-temporal evolution of post-seismic landsliding after the 2008 Wenchuan earthquake. Remote Sens. Environ. 236, 111476. https://doi.org/10.1016/j.rse.2019.111476.

Zhang, G., Cui, P., Jin, W., Zhang, Z., Wang, H., Bazai, N.A., Li, Y., Liu, D., Pasuto, A., 2021a. Changes in hydrological behaviours triggered by earthquake disturbance in a mountainous watershed. Sci. Total Environ. 760, 143349. https://doi.org/10.1016/j.scitotenv.2020.143349.

Zhang, Y., Song, C., Sun, G., Band, L.E., McNulty, S., Noormets, A., Zhang, Q., Zhang, Z., 2016. Development of a coupled carbon and water model for estimating global gross primary productivity and evapotranspiration based on eddy flux and remote sensing data. Agric. for. Meteorol. 223, 116–131. https://doi.org/10.1016/j.agrformet.2016.04.003.

Zhang, Y., Dannenberg, M.P., Hwang, T., Song, C., 2019a. El Niño-Southern oscillation-induced variability of terrestrial gross primary production during the satellite era. J. Geophys. Res. Biogeosciences 124, 2419–2431. https://doi.org/10.1029/2019JG005117.

Zhang, K., Song, C., Zhang, Y., Zhang, Q., 2017. Natural disasters and economic development drive forest dynamics and transition in China. For. Policy Econ. 76, 56–64. https://doi.org/10.1016/j.forpol.2015.08.010.

Zhang, Y., Song, C., Band, L.E., Sun, G., 2019b. No proportional increase of terrestrial gross carbon sequestration from the greening earth. J. Geophys. Res. Biogeosciences 124, 2540–2553. https://doi.org/10.1029/2018jg004917.

Zhang, J., Zhang, Y., Sun, G., Song, C., Dannenberg, M.P., Li, J., Liu, N., Zhang, K., Zhang, Q., Hao, L., 2021. Vegetation greening weakened the capacity of water supply to China's south-to-north water diversion project. Hydrol. Earth Syst. Sci. 25, 5623–5640. https://doi.org/10.5194/hess-25-5623-2021.

Zhang, J., Zhang, Y., Sun, G., Song, C., Li, J., Hao, L., Liu, N., 2022. Climate variability masked greening effects on water yield in the yangtze river basin during 2001–2018. Water Resour. Res. 58, e2021WR030382. https://doi.org/10.1029/2021WR030382.

Zhou, S., Yu, B., Huang, Y., Wang, G., 2014. The effect of vapor pressure deficit on water use efficiency at the subdaily time scale. Geophys. Res. Lett. 41, 5005–5013. https://doi.org/10.1002/2014GL060741.

Zhu, Z., Piao, S., Myneni, R.B., Huang, M., Zeng, Z., Canadell, J.G., Ciais, P., Sitch, S., Friedlingstein, P., Arneth, A., Cao, C., Cheng, L., Kato, E., Koven, C., Li, Y., Lian, X., Liu, Y., Liu, R., Mao, J., Pan, Y., Peng, S., Peñuelas, J., Poulter, B., Pugh, T.A.M., Stocker, B.D., Viovy, N., Wang, X., Wang, Y., Xiao, Z., Yang, H., Zaehle, S., Zeng, N., 2016. Greening of the earth and its drivers. Nat. Clim. Change 6, 791–795. https://doi.org/10.1038/nclimate3004.